Conductive MOFs: Synthesis and Applications in Supercapacitors and Batteries
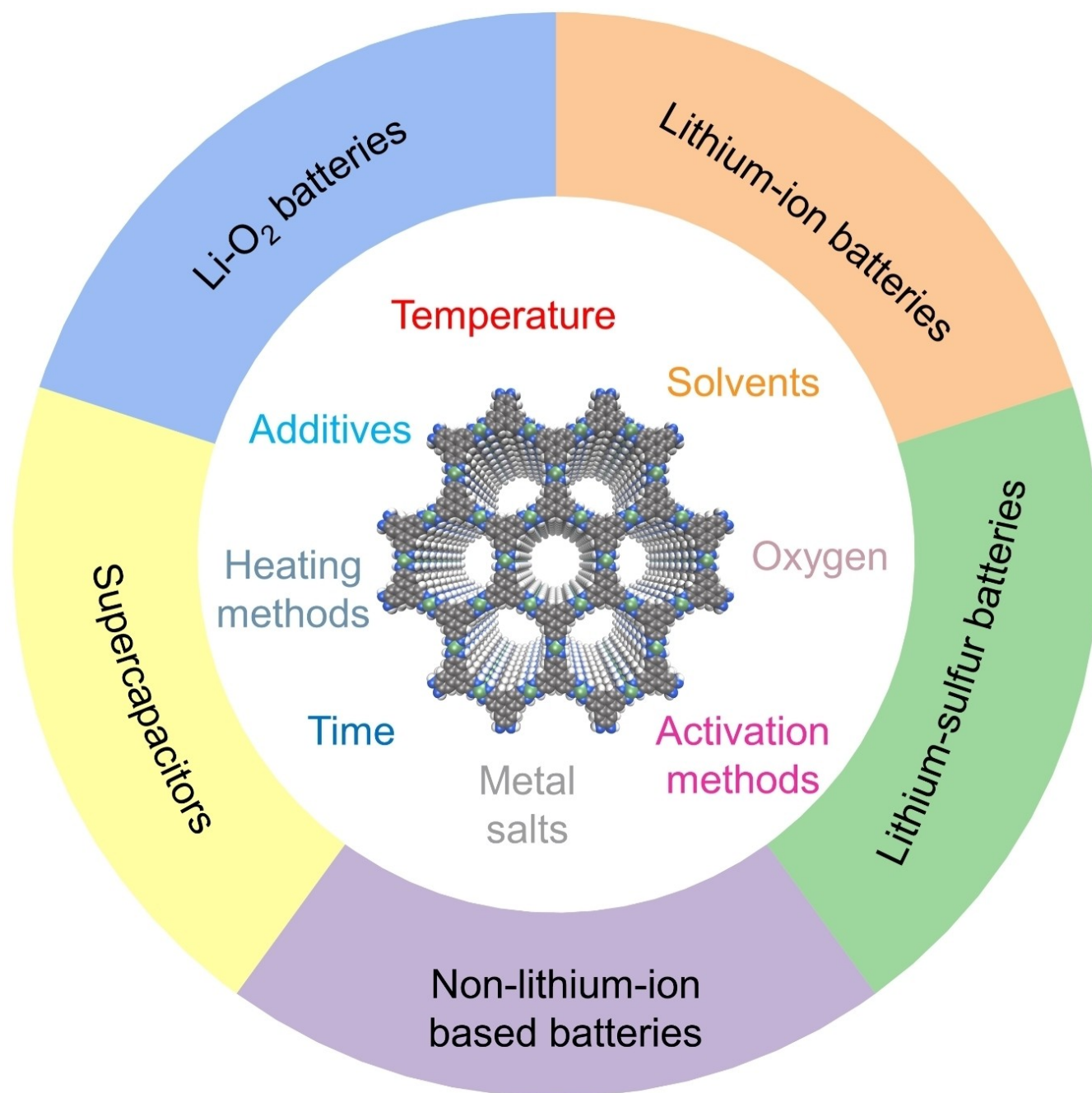
Pan Duan,[a] Wenlei Dai,[a] Zixuan Wang,[a] Ming Chen,[a] Liang Niu,[a] Taizheng Wu,[a] Liang Zeng,[a] and Guang Feng*[a]

Batteries & Supercaps

Review
doi.org/10.1002/batt.202300536

Chemistry Europe
European Chemical
Societies Publishing

Conductive metal-organic frameworks (c-MOFs) have uniform, adjustable pore sizes and customizable functional groups and excellent electrical conductivity, making them promising electrode materials for electrochemical energy storage. However, the synthesis of high crystallinity c-MOFs remains a significant challenge. The purpose of this review is to provide guidance for the synthesis of high crystallinity c-MOFs and emphasize their applications in the field of energy storage. We begin with reviewing the influence of various reaction conditions on the morphology, size, and crystallinity of c-MOFs, and then summarize the current work on c-MOFs in the field of electrochemical energy storage from both experiment and modeling. Furthermore, the existing issues are discussed in the development of c-MOFs and the primary directions for future research.

1. Introduction

An urgent need has been put forward for electrochemical energy storage systems as a result of the extensive growth of wind energy, solar energy, and other clean renewable energy sources, as well as the pervasive utilization of electronic gadgets like mobile phones, laptops, and electric vehicles.[1] Supercapacitors and batteries are among the popular electrochemical energy storage technologies, however, a fundamental trade-off exists between their ability to simultaneously achieve high power density and high energy density.[2] To ameliorate their performance, it is effective to choose appropriate electrode materials based on their energy-storage principles.[3] The electrode materials employed in these electrochemical energy storage devices are beset by various challenges.[4] For instance, in the case of electrical double-layer capacitors (EDLCs), energy storage in EDLCs is achieved by the adsorption of ions on the electrode surface through electrostatic interactions. The electrode materials for currently commercialized EDLCs are primarily made of porous carbons, which are favored because of their readily available raw materials, low cost, large specific surface area, and high conductivity.[5] However, they simultaneously face several challenges. The uneven pore size distribution makes it difficult for some ions to penetrate, thus preventing the full utilization of their surface area. The existence of a significant number of dead pores results in poor interconnectivity between pores, which is not conducive to the rapid transportation of ions during the charge and discharge process. The amorphous nature of activated carbon further complicates computational modeling and its integration with experimental investigations aimed at elucidating energy storage mechanisms.

Metal-organic frameworks (MOFs), initially emerged as Coordination Polymers (CPs) around the 1960s, are crystalline materials formed through coordination bonds between metal ions and organic ligands.[6] The work of Kitagawa,[7] Robson,[8] Yaghi,[9] Férey[10] and others in the 1990s progressively brought MOFs to the public and sparked a great deal of curiosity. MOFs have found extensive applications in gas storage, separation, and catalysis owing to their advantages of ultra-high specific surface area, large pore volume, and adjustable pore size.[11] However, traditional MOFs generally suffer from poor conductivity, limiting their further application in the electrical energy storage. The emergence of c-MOFs in recent years has unveiled their substantial potential as electrode materials for electrical energy storage.[12] However, the nascent development of c-MOFs is hampered by various unresolved issues.[13] While traditional MOFs boast remarkably high theoretical specific surface areas,[14] with experimentally synthesized MOFs surpassing 6000 m²/g,[15] the synthesized c-MOFs to date typically fall short, with surface areas averaging below 1000 m²/g.[16] Given that the electric conduction mechanism remains enigmatic to this day, the design and synthesis of new c-MOFs with a high specific surface area continue to be a significant challenge.[17] However, it is of utmost importance to develop new c-MOFs that possess super high specific surface area along with good conductivity for further improving the performance of energy storage devices. On the other hand, the synthesized c-MOFs commonly exhibit issues such as lower crystallinity and impurities within the pores. High crystallinity c-MOFs mean that the synthesized c-MOFs are closer to perfect crystals, and the reduction of amorphous phases, internal defects, and residual impurities in the crystals gives them a higher specific surface area (close to the accessible surface area).[18] A larger specific surface area can provide more ion adsorption sites or active sites, thereby improving the theoretical capacity. Furthermore, c-MOFs with a higher degree of crystallinity offer a wider voltage window, which is crucial for energy storage devices.[19] Both of these two factors can enhance the energy density. Moreover, the reduction of residual impurities in the pores can further facilitate ion transportation, thereby enhancing the power density. But in fact, due to the numerous influencing factors of the reaction conditions and the complex relationship between the reaction products and conditions, the synthesis of high crystallinity c-MOFs presents a significant challenge.

A few reviews on c-MOFs are already in existence, primarily focusing on conduction mechanisms, synthesis methodologies, and applications.[20] However, there is still a gap in systematically reviewing the parameters of various reaction conditions of c-MOFs and their relationship with the resulting products, especially regarding the attainment of high crystallinity in c-MOFs. Therefore, we decided to review the relationships between various reaction conditions and the resulting products. First, we delve into a detailed discussion of how specific reaction parameters influence the crystallization process. Subsequently, we thoroughly explore the applications of c-MOFs in supercapacitors and batteries to date. Finally, we present our perspective on the potential future developments of c-MOFs.

[a] P. Duan, W. Dai, Z. Wang, M. Chen, L. Niu, T. Wu, L. Zeng, G. Feng
    Huazhong University of Science and Technology Wuhan 430000 China
    E-mail: gfeng@hust.edu.cn

2. The influence of reaction conditions

The synthesis of c-MOFs encompasses a diverse range of reaction conditions that significantly impact the resultant topological structure, crystal morphology, size, and crystallinity of MOFs. However, unraveling the complex relationship between reaction products and their corresponding conditions remains a formidable challenge.[21] High crystallinity c-MOFs are typically generated through trial-and-error methods, as well as relying on personal chemical intuition and experience, which renders the synthesis process challenging. Hence, a comprehensive understanding and summarization of the influence exerted by various reaction parameters on synthesis becomes particularly critical. In the following sections, we will conduct an in-depth review exploring the impact of different reaction conditions on the characteristics of synthesized c-MOFs, including temperature, solvents, additives, reaction time, heating methods, types of metal salts, oxygen, and activation methods.

2.1. Reaction Temperature

The reaction temperature is admittedly one of the most pivotal factors in the synthesis process, exerting a multifaceted influence on the crystallization process of MOFs. This influence is manifested through various conceivable mechanisms, encompassing but not limited to the direct impact on nucleation and growth rates from a thermodynamic perspective,[22] the modulation of supersaturation levels and consequent reaction kinetics,[23] affecting dimensions,[24] affecting dielectric properties, and changing the pH of the solution.[25]

Temperature can affect the structure and morphology of c-MOFs by influencing bond formation. Dinca's group[26] found the effect of temperature on crystal morphology in the synthesis of M-HHTT (M = Cu, Co, Ni, Mg, HHTT = 2,3,7,8,12,13-hexahydroxyltetraazanaphthotetraphene). Under lower temperatures, the growth of the aforementioned four c-MOFs is mainly dependent on the coordination bonds between metals and ligands within the plane. The π-π interactions between the planes are relatively weak, leading to a predilection for in-plane growth, and thus resulting in the formation of plate-like particles. However, as the temperature increases, the π-π interactions between the planes intensify, encouraging inter-layer stacking and culminating in the formation of rod-like morphology. In addition, Qin et al.[27] successfully demonstrated the manipulation of Iron-Quinoid c-MOF morphology and crystallinity by changing the reaction temperature, in the microwave-assisted synthesis. Specifically, the Iron-Quinoid c-MOF crystal in dimethylformamide (DMF) solution may grow through coordination bonds within the plane and hydrogen bonding between planes. These two processes necessitate distinct thermodynamic conditions. Lower temperatures (140 °C) favor the induction of the hydrogen bonding, leading to the formation of plate-like stacked structures. Conversely, higher temperatures (170 °C) render interlayer hydrogen bonding notably unstable, thereby impeding the formation of stacked structures. Guided by this principle, plate-like and flower-like c-MOF particles were synthesized under conditions of 140 and 170 °C, respectively.

The size of the produced c-MOFs can be impacted by temperature as well. Park's group[28] demonstrated precise control over the particle size by manipulating the reaction temperature to regulate the rate of c-MOF nucleation and growth. Specifically, they conducted the synthesis of Cu-HHTC (2,3,8,9,14,15-hexahydroxyltribenzocyclyne) c-MOF under temperatures of 30, 40, 50, and 60 °C. Analysis of X-ray diffraction (XRD) results revealed a diminishing trend in the half-width of the diffraction peak as the temperature increased. Furthermore, the length and diameter of particles were statistically analyzed through scanning electron microscopy (SEM) and transmission electron microscopy (TEM), both of which showed a trend of increasing as the temperature rose. This observation indicates that increasing the temperature effectively promoted the particle size without sacrificing crystallinity.

2.2. Solvents

Solvents indeed exert a profound influence on the c-MOF synthesis, primarily by modulating the solubility of reactants, thereby affecting supersaturation, the nucleation and growth process, and ultimately resulting in distinct crystal shapes, sizes, and dimensions.[23] The effects of the solvent include the following, as a counter-ion to balance charge, it merges into the framework, affecting the size of pores and even the spatial structure,[29] altering the pH value of the solution and the
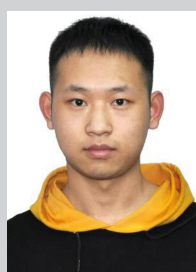
Pan Duan received his B.S. from Northeast Electric Power University in 2020. He is currently a graduate student in Huazhong University of Science and Technology. His research interests lie in the synthesis and application of three-dimensional conductive MOFs.

Guang Feng received his Ph.D. in 2010 from Clemson University (USA). From 2010 to 2013, he worked in Vanderbilt University (USA) as a postdoctoral research associate and then a research assistant professor. Since November 2013, he has been a professor in Huazhong University of Science and Technology (China). His research interests are focused on molecular modeling of interface and transport phenomena in electrochemical energy storage and capacitive deionization for desalination. He was selected as a Fellow of the Royal Society of Chemistry in 2019 and now serves as an associate editor of Energy Advances.

deprotonation rate of the ligand,[30] and modifying the surface tension of nanoparticles through dipole moment action, thereby influencing the appearance of crystal particles[31]

Solvents, by their ability to modify solubility, play a pivotal role in governing reaction rates. The incorporation of DMF as a co-solvent was found to yield Co-HAB (hexaaminobenzene) c-MOF with significantly heightened crystallinity in comparison to the use of water as the sole solvent. This enhancement is ascribed to that DMF has inferior solvation ability, which consequently decelerates the growth rate while elevating its crystallinity. Additionally, a positive correlation between the conductivity and the crystallinity of the sample was established.[32] This is primarily attributed to the reduction in interparticle contact impedance within crystalline particles. Similar to findings in other related studies, the electrical conductivity of single-crystal c-MOFs is several orders of magnitude higher than that of powder samples.[33] Simultaneously, they achieved the highest crystallinity and the highest conductivity (1.57 S cm^{-1}) for Co-HAB-D under the condition of DMF/water (1:1, v/v).

The stacking arrangement of c-MOF is susceptible to alterations under different solvents. La$_4$(HTTFTB)$_4$, La(HTTFTB), and La$_4$(TTFTB)$_3$ (H$_4$TTFTB = tetrathiafulvalene tetrabenzoic acid) c-MOFs with different topological and stacking structures were effectively executed by adjusting the ratios of mixed solvents (DMF, ethanol, H$_2$O), as illustrated in Figure 1(A–F).[34] With the

increase of the H$_2$O/DMF ratio, a greater degree of π-π overlaps became evident in the three structures, aligning with the stability provided by π-π interactions in solution and solid state. Such effect is because an increase in water content can cause instability in π-π interactions, necessitating more π-π stacking to reduce the system's energy and enhance stability. Subsequently, the same group found that solvent had a significant impact on the aggregation of HHTT molecules in the synthesis of Cu$_3$HHTT$_2$ and Co$_6$HHTT$_3$ c-MOFs. Dimethyl sulphoxide (DMSO) < DMF < 1,3-Dimethyl-2-imidazolidinone (DMI) was found to be the order of strength at which the solvent could disrupt the π-π stacking between the layers. Plate-like morphology is promoted by the application of solvents that have stronger disruption of π-π stacking.[26] Building upon the aforementioned work, it means more π-π stacking plate-like c-MOFs require the use of solvents with stronger π-π interactions (such as H$_2$O and DMI).

The coordination state of metal ions is another aspect that can be affected by the choice of solvent.[35] It was found that the original 2D layered structure could be translated into a three-dimensional (3D) framework by inserting the organic ligand nitrogen-containing 4,4-bipyridyl (BPY) as a pillar ligand into Cu-THQ (tetrahydroxy-1,4-benzoquinone) c-MOF. Cu^{2+} ions possess an affinity for planar square and spatial octahedral coordination. The incorporation of BPY ligands tends to coordinate with Cu^{2+} in the Cu-THQ plane, thereby trans-
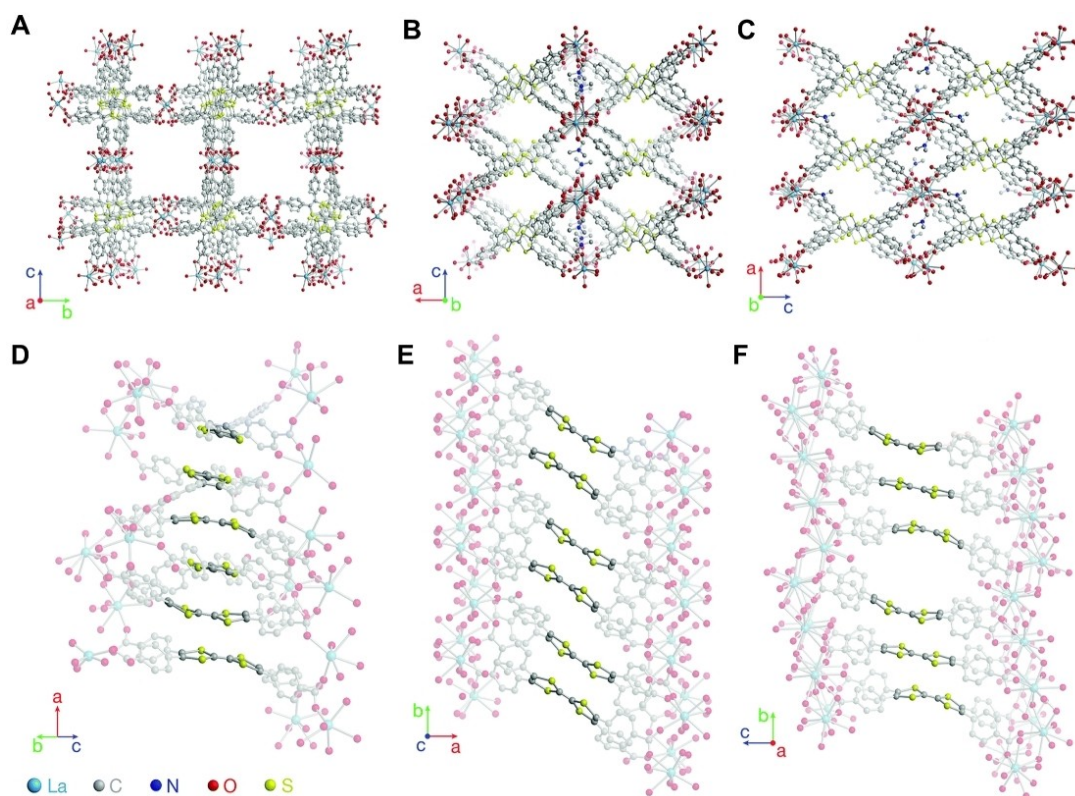

Figure 1. Solvent effect on the synthesis of c-MOFs. (A–F) Crystal structures of La$_4$(HTTFTB)$_4$, La(HTTFTB), and La$_4$(TTFTB)$_3$.[34] Copyright 2019 Royal Society of Chemistry. (A–C) Structures viewed along the channels, displaying the two types of pores in each c-MOF. (D–F) representations emphasizing the TTF stacking sequences and infinite La-carboxylate chain inorganic secondary building units (coordinated solvent molecules are omitted for clarity). All H atoms are omitted for clarity.

Batteries & Supercaps

Review
doi.org/10.1002/batt.202300536

Chemistry
Europe

European Chemical
Societies Publishing

forming the planar coordinated Cu^{2+} into octahedral coordination. In the process of inserting BPY ligands, it was observed that different solvents had a significant impact on the insertion effect. Water and DMF were used as solvents for synthesis respectively, and XRD results showed that the c-MOF had a higher degree of crystallinity by changing the solvent from DMF to water. This suggests that compared to DMF, water is more conducive to the occurrence of the insertion reaction, but the specific mechanism is still unclear.

2.3. Metal salts

Metal salts, as one of the raw materials for the synthesis of c-MOFs, undoubtedly play an important role in the crystal growth process. The commonly used metal cations in the synthesis of c-MOFs mainly include transition metals, such as Ni, Cu, Co, Fe, Mn, and La series metals.[36] The synthesis of various c-MOFs is frequently achieved by devising new ligands and pairing them with different metal cations. The impact of metal cations on the reaction mainly includes preferred coordination numbers and different geometric shapes,[37] kinetic characteristics (different ligand exchange rates),[38] and formed different clusters.[39] In addition, although anions do not directly participate in the reaction, they can also have a significant impact on the synthesis, such as affecting the nucleation rate, thereby affecting the size of the crystal,[40] affecting the shape of the crystal, and even the way the crystal grows.[41]

Different metal cations may result in various clusters, which makes the synthetic steps of c-MOFs based on different metal atoms of the same ligand potentially large gaps. When synthesizing c-MOFs using ligands with amino functional groups, deprotonation of the ligand and subsequent partial oxidation are often achieved by adding ammonia. Typically, the ammonia is first mixed with the Ni /Cu metal salt, then with the HAB ligand, and finally get Ni/Cu-HAB c-MOF.[42] However, in the synthesis of Co-HAB, it was found that Co^{2+} has a stronger affinity for OH^- than Cu^{2+} and Ni^{2+}, resulting in the formation of $Co(OH)_2$ impurities.[32] Consequently, they initiated the process by blending HAB with Co(II) salts in water, followed by the addition of ammonia to synthesize the Co-HAB c-MOF.

Furthermore, metal salts may have a crucial impact on the stacking structure (AA and AB stacking modes) of c-MOFs. The hexahydroxytriphenylene (HHTP) ligand is a common ligand in c-MOFs. Based on this ligand paired with different metal cations, a series of c-MOFs (Cu/Co/Ni-HHTP) have been successfully synthesized so far.[36b,43] Among them Cu-HHTP shows an AA stacking mode. However, when the metal atoms are replaced with Co or Ni, the stacking mode will vary greatly under similar synthesis conditions.[43a] Yaghi and co-workers[43a] discovered the presence of two crystallographically independent metal atoms within the crystal, both existing in an octahedral coordination environment by employing synchrotron radiation to conduct single-crystal X-ray diffraction studies on the synthesized Co-CAT-1. One of them coordinates with two adjacent HHTP ligands and two water molecules, forming a two-dimensional extended layer with hexagonal pores. The

other atom only coordinates with one HHTP ligand and four water molecules, resulting in an octahedral coordination structure forming discrete units. This extended layer and the intercalated layer composed of metal-covered HHTP alternate stacking to form an AB stacking mode. Similar phenomena have also appeared in 2,3,6,7,10,11-hexaiminotriphenylene (HITP)-based c-MOFs.[20c,33a,44] Moreover, Dinca's group[26] synthesized a series of c-MOFs using HHTT ligands with different divalent transition metal nodes (Cu^{2+}, Ni^{2+}, Mg^{2+}, and Co^{2+}). The resulting c-MOFs revealed various stacking modes because different metal atoms have varied preferences for planar square coordination and spatial octahedral coordination. Planar coordination, which was favored by Cu^{2+} and Ni^{2+}, resulted in the creation of M_3HHTT_2 c-MOFs with an eclipsed stack stacking mode and one-dimensional pores. Conversely, Co^{2+} and Mg^{2+} encouraged octahedral coordination, resulting in the creation of M_6HHTT_2, which displayed a staggered ABC stacking model, which consequently resulted in the disappearance of the pore structure.

2.4. Additives

Additives are often used to regulate the environment of the reaction to obtain the target product.[45] Based on their different functions, additives can be divided into modulators, surfactants, and hard templates.[46] Among them, the use of modulators is particularly widespread, and their modulation mechanisms can be further divided into deprotonation modulation[47] and coordination modulation.[48]

The deprotonation modulation is primarily accomplished through the pH adjustment of the solution by the addition of additives. A vertically extended structure 2D-vc-MOF(Cu) based on Cu^{2+} and HHTC ligand was created by Wang and co-workers.[45a] They systematically investigated the impact of different dosages of NaOH on crystallinity by adding 0, 1, 5, 10, and 20 ml of 4 M NaOH respectively. c-MOFs presented lower crystallinity were showed by XRD when the addition is 0 and 20 ml. This implies the existence of an optimal pH value in synthesis.

Coordination modulators can be used to control the size and morphological structure of crystals.[45b,c] Ultra-thin graphene-like c-MOF sheets were successfully synthesized by adding benzoic acid.[45b] The addition of benzoic acid can promote the coordination of the ligand porphyrins and the central atom Cu, causing charge repulsion between the c-MOF layers, and thereby reducing the stacking between the layers. Further increasing the amount of benzoic acid, the 'edge-to-edge' of the c-MOF sheets gradually decreases, promoting the anisotropic growth of the sheets, thus forming ultra-thin micron-level graphene-like. Brozek's group[45c] obtained Fe(TA)2 (TA = 1,2,3-triazole) nanocrystals with a minimum size of only 5.5 nm by controlling the amount of modulator. They added 1-methylimidazole (1-mIm) as a modulator, which forms a secondary building unit similar to the TA ligand by competing for coordination with the TA ligand and iron ions. However, the single linkage on the surface of this secondary building unit

Batteries & Supercaps

Review
doi.org/10.1002/batt.202300536

Chemistry
Europe
European Chemical
Societies Publishing

(SBU) prevents further growth of the particles until it dissociates, therefore it also limits the size of the c-MOF particles. As the amount of 1-mlm increases, the resulting crystal size diminishes progressively (Figure 2(A–F)).

Similarly, Cu-HHTP c-MOFs of various morphologies were generated by researchers using the previously mentioned modulators.[49] Beyond confirming previous conclusions, this study revealed that the choice of additive could significantly affect the interlayer stacking structures. Two different stacking models, namely the eclipsed co-facial AA-stacking and the near-eclipsed staggered AA-stacking, were observed through XRD analysis. Under low 2θ diffraction peaks, only the c-MOFs synthesized using DMF as a modulator displayed clear peak splitting, suggesting a closer alignment to the near-eclipsed staggered AA-stacking model. On the other hand, the data from the remaining groups adhered more closely to the eclipsed co-facial AA-stacking model (as demonstrated in Figure 2(G–J)). This study is the first to illuminate the potential impact of modulators on interlayer stacking in 2D c-MOFs.

It's worth noting that modulators may simultaneously possess the aforementioned two types of modulation functions.[50] Different additives, such as alcohols, amines, azides, DMF, and tetrahydrofuran (THF), were utilized in varying concentrations to synthesize $Cu_3(HHTP)_2$ c-MOF films. Among them, alcohols, DMF, and THF resulted in low c-MOF yields (a lot of unreacted ligands), and only the desired c-MOF films
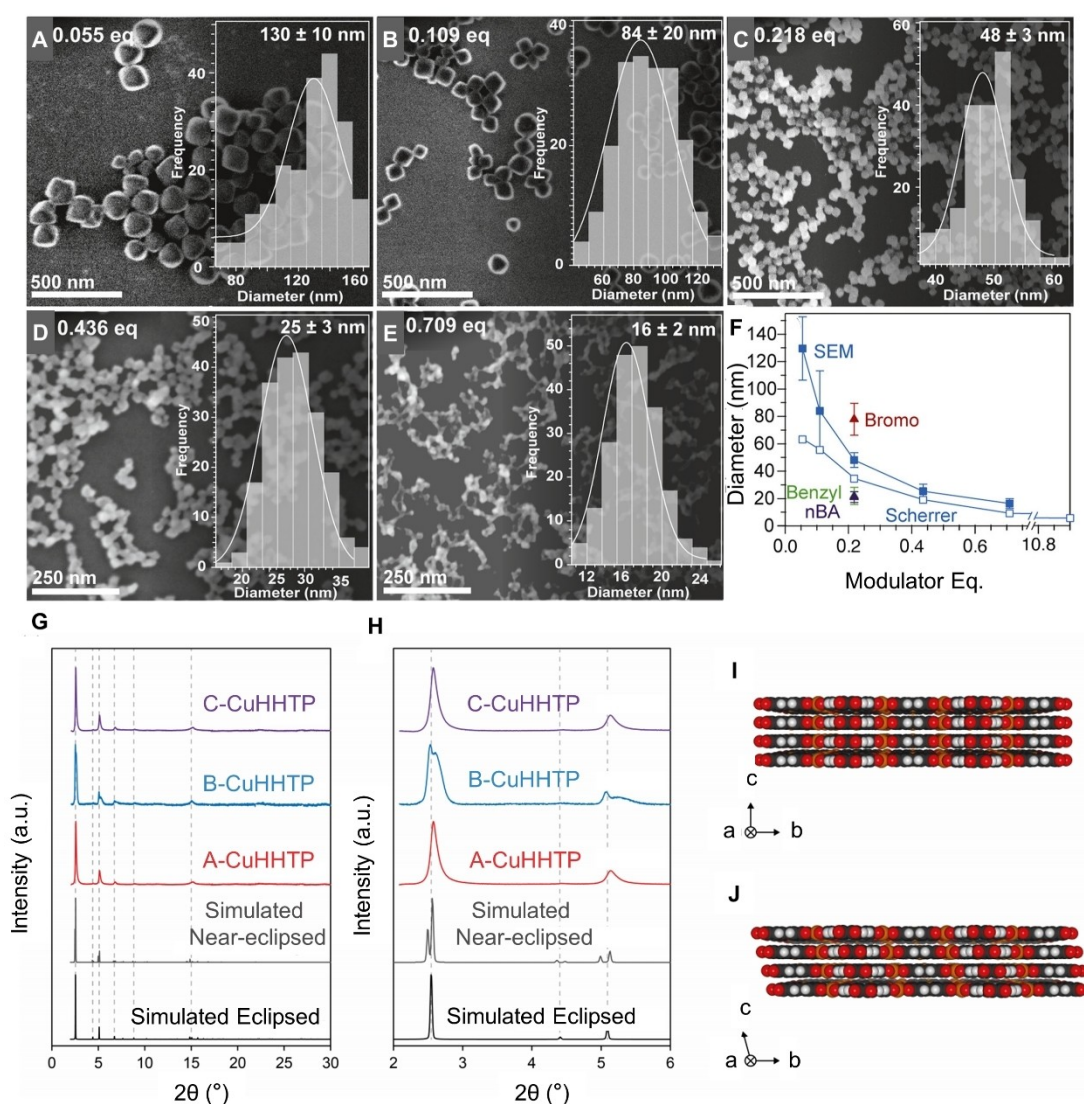

Figure 2. Additives effect on the synthesis of c-MOFs. (A–F) Particle sizes of $Fe(TA)_2$ resulting from modulated syntheses.[45c] Copyright 2022 American Chemical Society. (A–E) SEM images of $Fe(TA)_2$ nanoparticles synthesized with 1-mlm equivalents (with respect to $FeCl_2$) ranging from 0.055 equivalent (A) to 0.709 equivalent (E). Images were set to grayscale using Adobe Illustrator. Insets, histograms of particle size distributions from > 200 particles fitted to weighted Gaussian distributions. (F) Particle sizes using 1-mlm (blue squares), 1-benzyl-2-methylimidazole (benzyl, green triangle), 5-bromo-1-methylimidazole (bromo, red triangle), and n-butylamine (nBA, purple triangle). Filled data points were determined by SEM and open data points were by Scherrer analysis. (G–J) XRD patterns and structure of CuHHTP.[49] Copyright 2022 Royal Society of Chemistry. (G) Experimental XRD patterns from A-CuHHTP, B-CuHHTP, and C-CuHHTP compared to the simulated XRD patterns from $Cu_3(HHTP)_2$ with both eclipsed and near-eclipsed stacking sequences, and (H) zoomed view to show the differences in peak splitting and shape between the three samples. (I, J) Structural models of $Cu_3(HHTP)_2$ with hexagonal eclipsed and monoclinic near-eclipsed crystal structures, respectively.

Batteries & Supercaps

Review
doi.org/10.1002/batt.202300536

Chemistry
Europe
European Chemical
Societies Publishing

could be obtained when amines and pyridines were added. This was mainly because the solubility of the HHTP ligand may have increased due to the addition of amines and pyridines, which raises the pH. When pyridine was used as a modulator, only when 50 equivalents of pyridine were added, the product looked more like a film. In contrast, all the samples synthesized had a plate-like structure, under the conditions of adding ammonia, which were bound to the free coordination sites of Cu^{2+} in the original square coordination environment of the HHTP ligand. To facilitate crystal growth in the c direction, it was first necessary to remove these ammonia ligands. This resulted in a slower elongation rate of the crystal in this direction, culminating in the formation of a plate-like structure.

2.5. Reaction Time

It usually takes several hours to a few days to get MOFs by using the hydrothermal method.[51] This prolonged reaction time presents a significant challenge for MOF optimization. In many synthesis processes for single-crystal MOFs, the reaction rate is slowed down as much as possible to minimize the generation of defects during the coordination process, thereby obtaining large-sized MOF single crystals.[52] An extremely low reaction rate inevitably leads to an excessively long reaction time. However, without reducing the reaction rate, does merely prolonging the reaction time also enhance the crystallinity of the MOF? The answer to this question doesn't seem to be straightforward.

The effects of reaction time on the resultant c-MOFs can be roughly categorized into three types, reaction time has no impact on crystallinity, increasing reaction time may lead to a self-repair process to improve crystallinity, and extending reaction time could result in ligand dissolution, causing a decrease in crystallinity. In the synthesis of Cu-HHTC, Park's group[28] conducted extensive optimization of various parameters, including reaction time. Their reaction system was subjected to different durations, namely 4, 6, 8, and 12 hours, at 50 °C under 100 rpm stirring conditions. With the increase in reaction time, the crystallinity of the resultant c-MOF first increased and then decreased. This implies that there is an optimal reaction time, and extending the reaction period may have detrimental effects. Similar phenomena have been reported in other studies as well.[45a,53] Due to the limited number of relevant studies in c-MOFs, we haven't yet seen any reports where increasing reaction time either improves crystallinity or has no effect.

2.6. Heating methods

The vast majority of c-MOFs need to be synthesized under heating conditions, with traditional conductive heating (CE) including oil bath heating, sand bath heating, vacuum drying oven heating, and others.[16c,54] Non-traditional heating methods, such as microwave heating (MW) and ultrasound heating (US) are also employed.[27,55] Furthermore, considering the unique

conductivity of c-MOFs compared to other MOFs, electrochemical synthesis methods are noteworthy.[56] Even when only changing the heating method while keeping other reaction conditions the same, significant effects on yield, and crystal particle size and morphology can be observed.[57]

Traditional heating methods mainly employ heat conduction, for example, oil bath heating indirectly heats the reaction solution through oil as a heat transfer medium. Similarly, sand bath heating uses sand as the heat transfer medium. Just changing the heat transfer medium can have a significant impact on the reaction. For instance, Feng and co-workers[54b] found that even under the same temperature conditions, sand bath heating produced samples with significantly improved crystallinity compared to oil bath heating in the synthesis of $Ni_2[CuPc(NH)_8]$ ($CuPc(NH)_8 = 2,3,9,10,16,17,23,24$-octaaminophthalocyaninato copper [II]).

Microwave-assisted synthesis heats the reaction solution directly through the interaction of electromagnetic waves with mobile electric charges, which include polar solvents (such as water), metal ions, and deprotonated ligands.[57] This direct action makes microwave heating highly efficient, allowing for rapid crystal formation in a very short time. Consequently, microwave synthesis often requires very little time, usually less than an hour, which is an attractive advantage.[57] Ultrasonic synthesis uses ultrasonic waves (20–1000 kHz) to heat the reaction system. In particular, when ultrasonic waves are used on a liquid, bubbles begin to form in the solution. Once these bubbles reach a certain size, they begin to collapse and release a lot of energy, creating transient local hot spots (temperatures up to about 5000 K), which heat the surroundings.[58] Apart from reducing the reaction time, microwave and ultrasound synthesis can also produce smaller crystal particles. When the identical MOF is synthesized using conventional heating, microwave, and ultrasound irradiation, the particle size typically decreases in the following order, CE > MW > US.[46] To date, reports on the synthesis of c-MOFs using microwave heating and ultrasonic heating are quite rare, which is certainly worth noting for future research.

Compared to other synthesis methods, the uniqueness of electrochemical synthesis lies in the source of metal ions. Instead of being directly added, metal ions are supplied by corresponding metal electrodes through the application of voltage. This allows electrochemical synthesis to regulate the concentration of metal cations in the solution or control the possibility of metal oxidation states by controlling voltage and current, thereby manipulating the crystallization process. In 2021, a Cu-HHTP c-MOF film with excellent conductivity was successfully prepared by using an electrochemical synthesis method.[56] A cylindrical container was utilized as an electrolytic cell, with two copper foils designated as the anode and cathode, respectively. A blend of methanol and water, containing the HHTP ligand, was infused into the electrolytic cell, and ammonia was incorporated to expedite the dissolution and deprotonation of HHTP (Figure 3(A–B)).

After switching on the power supply and applying the appropriate voltage, the copper foil at the anode began to release copper ions, attracting the deprotonated ligand to react
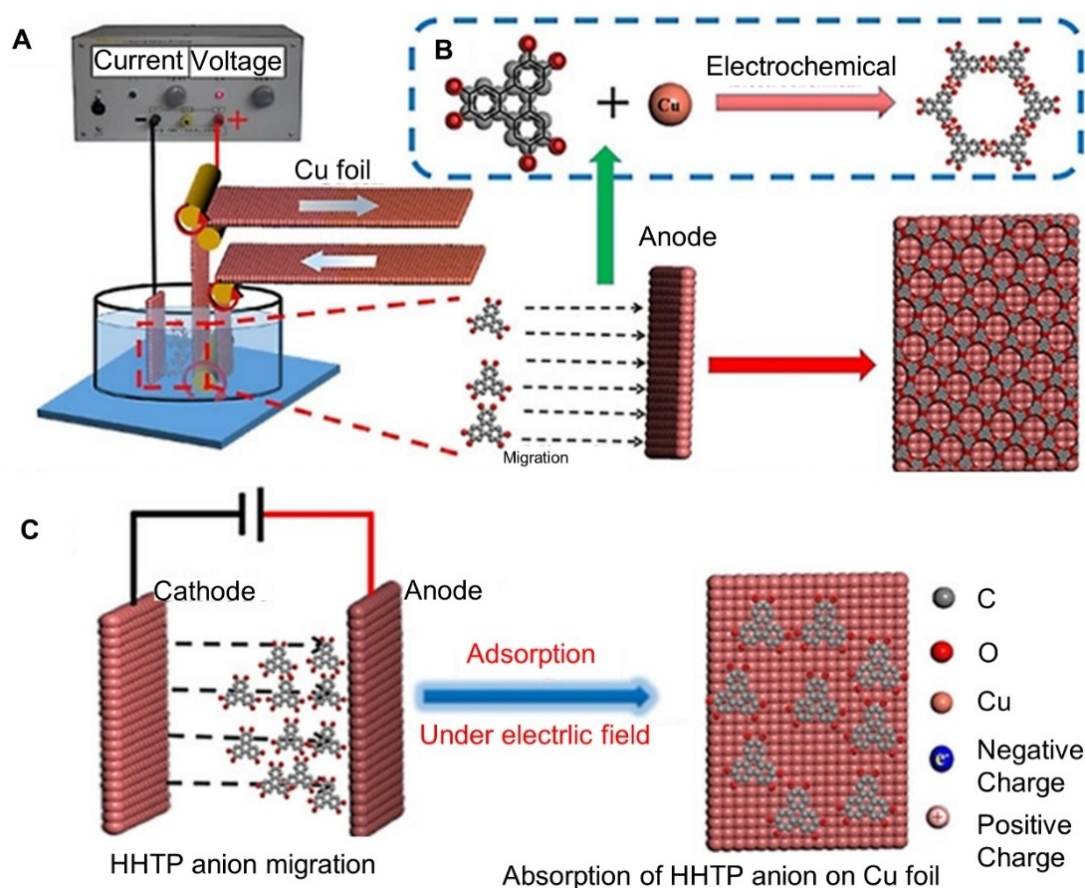
Batteries & Supercaps

Review
doi.org/10.1002/batt.202300536

Chemistry
Europe

European Chemical
Societies Publishing

Figure 3. Electrochemical synthesis of $Cu_3(HHTP)_2$ film.[56] Copyright 2020 Wiley-VCH GmbH. (A) Electrochemical reaction cell for the preparation of a $Cu_3(HHTP)_2$ film on Cu foil. (B) Schematic diagram of coordination reaction between Cu^{2+} and the HHTP ion. (C) Schematic diagram of HHTP anion migration in electric field and adsorption on Cu anode.

at the anode, generating a c-MOF film on the anode surface (Figure 3(C)). Under the influence of varying electrostatic interactions, distinct growth patterns emerged upon applying different voltages. At low voltages, a smaller volume of liberated Cu^{2+} underwent a reaction with the HHTP anion to yield negatively charged $[Cu_{3n}(HHTP)_{2n+a}]^{3a-}$ sheets. The electrostatic attraction between these sheets and the copper anode facilitated coordination reactions along the copper surface. Conversely, when a high voltage was applied, an excess release of Cu^{2+} interacted with the HHTP anion, giving rise to $[Cu_{3n+b}(HHTP)_{2n}]^{2b+}$ sheets. The resultant electrostatic repulsion caused a fraction of the sheets to detach from the anode surface. Continued growth under high voltage conditions led either to the formation of large c-MOF crystals on the anode surface or their release into the solution.

2.7. Oxygen

Oxygen has been identified to play an important role in the synthesis of c-MOFs.[59] Dinca et al. found that the presence of oxygen was indispensable when synthesizing $M_3(HIB)_2$ (M=Ni, Cu, HIB=hexaaminobenzene) MOF. If the reaction is carried out in air-isolated conditions, only an amorphous grey powder is

obtained.[59] Similarly, in the synthesis of $M_3(HITP)_2$ (M=Co, Cu, Ni), placing the reaction system in a nitrogen environment yielded no precipitate after three hours of reaction.[44] In 2022, the same group, using Ni^{2+} and 2,3,5,6-tetraamino-1,4-hydroquinone (TAHQ) ligands, synthesized frameworks from 1D, 2D to 3D with the same metal ion and ligand ratio by changing gas atmosphere during the reaction process.[60] The presence of oxygen could oxidize the two amines in TAHQ to form tetraaminobenzoquinone (TABQ). In TAHQ, both phenol and amine can coordinate with metal ions, but in TABQ, only amine can coordinate, leading to different dimensions of the final c-MOF.

The content of oxygen also has a significant impact on the synthesis. Wang and co-workers[45a] optimized the oxygen content in the reaction system during the synthesis of 2D-vc-MOF(Cu). They adjusted the volume of oxygen by switching to smaller bottles of different volumes, ultimately finding that under conditions with 1.5 ml of oxygen, the obtained c-MOF had the highest crystallinity. Particularly, when there was no oxygen, only copper oxide was generated, and no c-MOF was formed. Similarly, Wang's group[61] changed the bubbling conditions (oxygen content) to alter the reaction rate, finally obtaining a higher crystallinity Ni-BTA (1,2,4,5-benzene tetramine) c-MOF. They found that increasing the liquid/oxygen

Batteries & Supercaps

Review
doi.org/10.1002/batt.202300536

Chemistry Europe
European Chemical
Societies Publishing

interface through bubbling can accelerate the coordination reaction, thereby increasing the potential coordination of one Ni^{2+} with more than two BTA molecules, forming crosslinked coordination polymers, thus introducing more defects and reducing crystallinity.

Furthermore, even a small amount of dissolved oxygen in the solution can have a significant impact on the synthesis. Fe-HHTP c-MOF can only be obtained when both the metal salt solution and the ligand solution have been subjected to degassing treatment.[43b] The metal salt solution and ligand solution were separately degassed, and upon mixing them, it was observed that when oxygen was introduced to the metal solution under inert conditions before adding it to the ligand solution, the crystallinity of Fe-HHTP significantly decreased. This indicates that the highly redox-active Fe^{2+} is the source of high oxygen sensitivity.

2.8. Activation methods

After the reaction process of c-MOFs, it is usually necessary to clean and dry the resulting c-MOFs to remove unreacted ligands, additives, solvents, and other impurities that may exist in the pores of the c-MOFs. The activation process is an extremely important step in releasing the full potential of c-MOFs, but it is also an important process that is easily overlooked.[34] Recognizing the limited discussion in previous reviews,[20a,d,62] we choose to introduce this section in detail. Commonly used activation methods include heat and vacuum treatment,[63] solvent exchange,[64] supercritical carbon dioxide method,[65] freeze-drying method,[66] and photothermal activation.[67]

The most common activation method is solvent exchange followed by heating and vacuum treatment.[68] As for solvent exchange, the simplest method is to directly add the solvent to the obtained c-MOF powder, and then evenly disperse the particles in the solvent through stirring or ultrasonication, finally separate the solvent and c-MOF by centrifugation to achieve the purpose of cleaning. For example, Dinca's group[16b] dispersed the powder in water, methanol, and acetone in sequence, and completed the cleaning of possible impurities in the $Ni_3(HITP)_2$ c-MOF pores with centrifugation operations. To make the solvent exchange process more thorough, researchers may use long-time soaking[69] or reflux[33a] to enhance the exchange process of solvent molecules and substances in the c-MOF pores. It's worth noting that, during the solvent exchange process, the solvents used typically need to be selected in a way that decreases surface tension, the purpose of which is to avoid destroying the structure of the c-MOFs during the removal of solvent molecules due to the excessive interaction between the solvent molecules and the c-MOF. In the solvent exchange process, commonly employed solvents comprise DMF, H_2O, methanol, acetone, ethanol, DMSO, and others. The standard procedure involves an initial cleaning with solvents employed during the synthesis process, followed by the selection of cleaning solvents in descending order of solution polarity.[26] The solvents listed above, arranged in decreasing

order of polarity, are as follows: H_2O, DMSO, DMF, methanol, ethanol, and acetone.[70] After cleaning the impurities in the c-MOFs pores through the solvent exchange, it is necessary to further remove the solvent molecules remaining in the pores, and the specific treatment methods include, drying with nitrogen,[16b] heating vacuum drying,[51] dynamic vacuum treatment.[71] For some special cases, the above ways of removing solvent molecules are still too crude, and more gentle means are needed. For example, different structures of 1, 2, 3-La-HTTFTB c-MOFs were obtained. The common dynamic vacuum method could be used to activate 2-La-HTTFTB, but 1 and 3 lost crystallinity due to solvent removal when the dynamic vacuum was at 220 °C, necessitating the use of softer activation techniques. The crystal phases of 1 and 3 were eventually obtained through solvent exchange and drying using supercritical carbon dioxide.[34]

In addition to the above potential influencing factors, there are many other factors to be considered in the specific synthesis experiments, such as the experimental environment (e.g., room temperature and indoor humidity), the purity of the chemicals and their manufacturers, the materials and size of the reaction containers, the manufacturer of the heating equipment, the position of the reaction vessel in the heating apparatus, cooling rates and so on. One crucial aspect in the synthesis of c-MOFs is the choice of ligand. High-purity ligands are a necessary condition for the synthesis of high crystallinity MOFs, which is a major challenge in MOF synthesis. In this section, we have summarized the possible influencing factors and their potential impacts on the reaction and subsequent activation process of c-MOFs. We hope to give readers a comprehensive understanding of various experimental conditions and provide as many references and guidance as possible for obtaining high crystallinity MOF crystals.

3. Application of c-MOFs in electrochemical energy storage

c-MOFs have attracted more and more attention in the field of electrochemical energy storage due to their advantages such as high specific surface area, large number of active sites, regular pore structure, and good conductivity.[62b] Its main application areas can be divided into supercapacitors and batteries.

3.1. c-MOFs in supercapacitors

As early as 2017, Ni-HITP c-MOF pure electrode was first applied in supercapacitors, achieving excellent electrochemical performance.[12a] Within a two-electrode cell composed of organic electrolyte 1 M tetraethylammonium tetrafluoroborate (TEABF$_4$) in acetonitrile, it exhibited a specific capacitance of 111 F g^{-1} at a current density of 0.05 A g^{-1}. Simultaneously, the areal capacitance reached 18 µF cm^{-2}, with extremely low equivalent series resistance (0.47 Ω) and good cycling stability with a capacitance retention rate of 90% after 10000 cycles

Batteries & Supercaps

Review
doi.org/10.1002/batt.202300536

**Chemistry
Europe**
European Chemical
Societies Publishing

(Figure 4). Three Ni-HITP c-MOFs with distinct crystallinities were synthesized by Feng's group.[19] The corresponding specific surface areas increased to 556, 641, and 732 $m^2 g^{-1}$, respectively. The resulting electrode capacitances were observed at 58, 70, and 76 $F g^{-1}$, highlighting a clear positive correlation among crystallinity, specific surface area, and capacitance. Simultaneously, the increase in specific surface area from 556 to 732 $m^2 g^{-1}$ coincided with the expansion of the voltage window from 2.1 V to 2.8 V. This study establishes the crucial role of high crystallinity in c-MOFs for enhancing electrochemical performance. The electrochemical performance of c-MOFs is notably affected by the crystallinity, while the size and morphology of c-MOFs also exert significant influence. Various lengths of Ni-HITP c-MOFs were synthesized by Dincă's group[72] through alterations in additive types and reaction vessel sizes. The conductivity measurements revealed an inverse relationship between rod length and powder conductivity, with a discernible two-order magnitude difference. Additionally, distinctions were observed in the aggregation morphology of Ni-HITP c-MOFs with varying rod lengths. Longer rod resulted in entanglement, causing pore blockage and a pronounced reduction in specific surface area compared to the two other MOF variants with shorter rod lengths. Moreover, longer rod contributed to a decrease in specific surface capacitance and an increase in ion transport impedance, adversely impacting electrochemical energy storage. These findings underscore the necessity of controlling the size and morphology of Ni-HITP c-MOFs to optimize their electrochemical properties.

In addition to utilizing pure c-MOF as an electrode, many studies opt to enhance the electrochemical performance by growing c-MOFs on various substrates. Xu and co-workers[73] successfully cultivated Cu-CAT c-MOF on carbon fiber paper, forming a c-MOF nanowire array. This array was directly employed as electrode materials for the assembly of a solid-state supercapacitor. In comparison to pure Cu-CAT powder, both capacitance and rate performance witnessed significant improvements Zhou et al.[74] reported the fabrication of c-MOF nanolayers on cellulose nanofibers (CNFs) through interfacial synthesis, forming nanofibrillar CNF@c-MOF. These hybrid nanofibers, CNF@c-MOF, are easily assembled into freestanding films, exhibiting remarkable characteristics in high electrical conductivity (up to 100 $S cm^{-1}$), hierarchical micro/mesoporous structure, and excellent mechanical properties. Assembled into supercapacitors, they displayed outstanding cyclic stability, retaining over 99% capacitance after 10,000 consecutive charge-discharge cycles. This work suggests a promising pathway for developing flexible energy storage devices using sustainable cellulose and c-MOFs. More research on the use of c-MOFs in supercapacitors can refer to our previous review.[62b]

To better understand the energy storage mechanism of c-MOF-based supercapacitors, the quantum-mechanics/molecular-mechanics (QM/MM) technique was applied to investigate the charging mechanisms of $Cu_3(HHTP)_2$ incorporating 1 M $TEABF_4$ in acetonitrile electrolyte within the cylindrical pore.[75] The number of ions inside cylindrical pores was manipulated to alter the charging mechanism, i.e., either counter-ion insertion or co-ion removal (Figure 5A). The results showed that for both the positive and negative electrodes, higher capacitance was obtained when cations were the primary charge carriers. Subsequently, the simulation results were compared with experimental data, which shows that for both positive and negative electrodes, the capacitance values fell between the two charging mechanisms (Figure 5B). That indicated the reliability of the simulation results and suggested that cations were indeed the main charge carriers in reality. Furthermore, based on the ion distribution inside the pores, the voltage drop was decomposed into three components, explaining why larger mobility constants resulted in higher capacitance. When studying the charging mechanism of the $Cu_3(HITP)_2$ electrode, it was found that the drop in positive electrode potential decreased, and the capacitance significantly increased compared to $Cu_3(HHTP)_2$. This indicated that, although the two MOFs have similar pore structures and pore sizes, the functional groups of the ligands significantly influence the electrical double-layer structure and capacitance response.
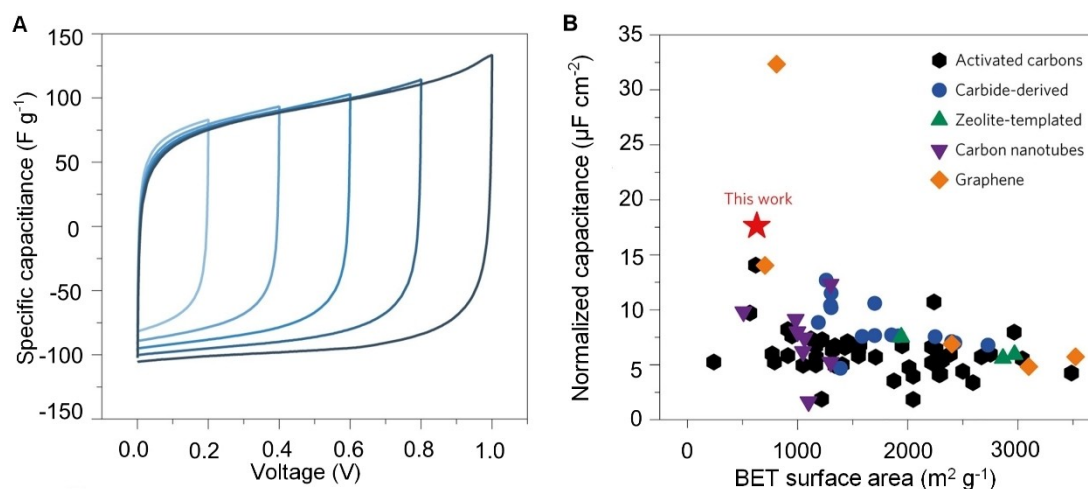

Figure 4. c-MOFs based supercapacitors.[12a] Copyright 2016, Springer Nature. (A) Cyclic voltammetry at a scan rate of 10 mV s^{-1} at increasing cell voltage. (B) Comparison of areal capacitance for various materials normalized relative to their BET surface areas.
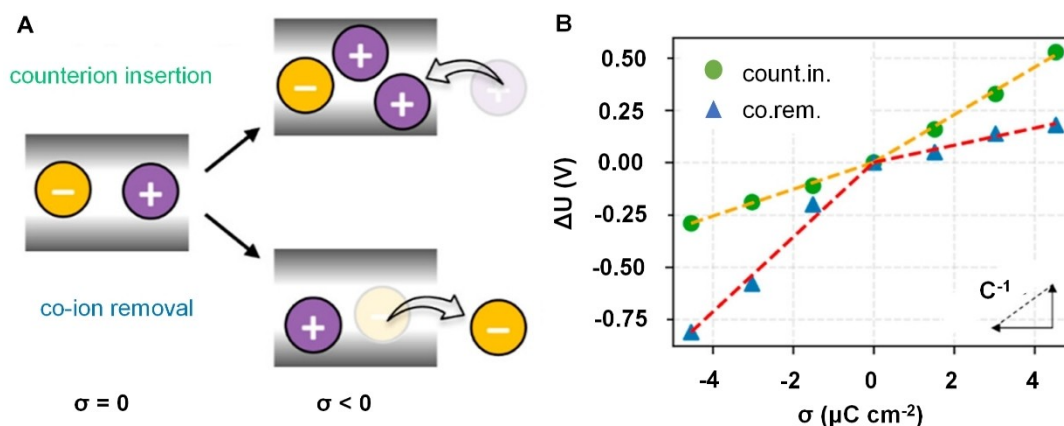
Figure 5. Energy storage mechanism of c-MOFs based supercapacitors.[75] Copyright 2023 The Authors. Published by American Chemical Society. (A) Schematic to show two primary charging mechanisms when the charge density σ < 0. The upper panel shows the counterion insertion (count.in.) mechanism, while the lower panel shows the co-ion removal (co.rem.) mechanism. (B) σ-ΔU curve along two different charging mechanisms. The slope indicates the inverse C.

It's worth noting that the c-MOFs that have been successfully applied to supercapacitors are all 2D structures, and there are currently no reports of 3D c-MOFs being used in EDLCs. 3D c-MOFs have higher theoretical specific surface areas than 2D c-MOFs, which allows them to offer more ion adsorption sites and, as a result, exhibit higher capacitance.[19] Moreover, 3D c-MOFs have more developed ion transport channels, which are more conducive to ion transport compared to the one-dimensional pore structure of 2D c-MOFs. However, the application of 3D c-MOFs in EDLCs is currently hindered by the following issues, 1) Most 3D MOFs are non-conductive, and the number of reported 3D c-MOFs is still limited. 2) Existing 3D c-MOFs have difficulty balancing good conductivity and porosity. 3) Certain 3D c-MOFs possess only one-dimensional (1D) pore structures. 4) Some 3D c-MOFs have residual solvent molecules and other impurities in their pores, which limits their application in certain electrolyte systems (such as c-MOFs containing water molecules, which are difficult to apply in ionic liquid and organic electrolyte systems).

In 2009, the first 3D c-MOF, $Cu[Cu(pdt)_2]$ (pdt = 2,3-pyrazine-dithiolate) was reported, which had a conductivity of 6×10^{-4} S cm^{-1} at 300 K but lacked a porous structure.[76] In 2010, Long and co-workers reported the first porous 3D c-MOF, $Cu[Ni(pdt)_2]$. It had a room temperature conductivity of 10^{-4} S cm^{-1}, but its specific surface area was only 385 m^2 g^{-1}, which was even lower than some 2D c-MOFs.[77] In 2015, the same team successfully synthesized the mixed-valence ligand-based MOF $(NBu_4)_2Fe^{III}_2(dhbq)_3$ (dhbq$^{2-/3-}$ = 2,5-dioxidobenzo-quinone/1,2-dioxido-4,5-semiquinone). Due to the presence of dhbq^{2-} and dhbp^{3-}, its room temperature conductivity reached up to 0.16 S cm^{-1}. However, based on nitrogen adsorption tests, no pore presence was detected.[78] Not until 2018 was a 3D c-MOF, $K_xFe_2(BDP)_3$ (BDP^{2-} = 1,4-benzenedipyrazolate), that balanced relatively high conductivity (10^{-3} S cm^{-1}) and a relatively high specific surface area (1230 m^2 g^{-1}) reported. However, this c-MOF had a 1D pore structure, rather than a 3D pore structure.[79] Similarly, in 2018, Dinca's group[80] reported the then highest conductivity 3D c-MOF, $Fe_2(BDT)_3$. By adjusting the

proportion of Fe^{2+} and Fe^{3+}, its conductivity could exceed 1 S cm^{-1}, but it only had a modest Brunauer–Emmett–Teller (BET) surface area of 614 m^2 g^{-1}. In 2021, Medina and co-workers[71] reported a 3D c-MOF, Fe-HHTP, which combined conductivity and porosity along with a 3D pore structure. It had a room temperature conductivity of 10^{-3} S cm^{-1} and a specific surface area exceeding 1400 m^2 g^{-1}, but its internal large amount of crystalline water limited its application. In 2023, Wang's group[81] reported a highly conductive 3D conjugated coordination polymer (CCP), Cu-TAPT (2,3,7,8-tetra-aminophenazine-1,4,6,9-tetraone). The crystal structure consists of one-dimensional π-d conjugated chains within the plane. The tight π-π interactions between adjacent chains are bridged by another column of stacked chains, forming a 3D CCP with high conductivity, achieving a room temperature conductivity of 400 S cm^{-1}. Different from the previously reported $(NBu_4)_2Fe^{III}_2(dhbq)_3$ MOF,[78] Takaishi and co-workers[82] synthesized the $Fe_2(dhbq)_3$ c-MOF, which only contains dhbq^{2-}. Owing to the lack of charge transfer between ligands induced by mixed valence dhbq$^{2-/3-}$, it exhibits a relatively lower conductivity of 1.2×10^{-2} S cm^{-1}. However, as there is no longer any NBu^{4+} in the pores, it possesses a larger Langmuir surface area of 556 m^2 g^{-1}. There is a significant discrepancy from the previously predicted theoretical surface area of 5070 m^2 g^{-1}. It remains unclear whether this is due to a low degree of crystallinity in the synthesized c-MOF, insufficient activation, or a problem with the theoretical prediction. The detailed parameters such as conductivity, specific surface area, band gap, and others can be found in Table 1. Although 3D c-MOFs are attracting increasing attention, the work related to their synthesis is still relatively scarce, and further efforts are needed.

3.2. c-MOFs in Batteries

In 2018, Nishihara and co-workers[98] successfully applied the metallically conductive bis(diimino)nickel framework (NiDI) to LIBs. Research showed that NiDI possesses three kinds of redox

Table 1. Properties of 3D c-MOFs.

Name of c-MOF	σ [S cm^{-1}] (300 K)	Method	SSA (m^2 g^{-1})	Pore size (Å)	Electronic band gap (eV)	Band gap (eV)	Ref.
Cu[Cu(pdt)$_2$]	6×10^{-4}						[76]
Cu[Ni(pdt)$_3$]	10^{-8}–10^{-4}	a	385			2	[77]
MET-3	0.77×10^{-4}	e	450	4.54			[83]
(NBu$_4$)$_2$Fe$^{III}_2$(dhbq)$_3$	0.16	a					[78]
Na$_{0.9}$(NBu$_4$)$_{1.8}$Fe$^{III}_2$(dhbq)$_3$	6.2×10^{-3}	a					[78]
Mn$_2$(TTFTB)	8.64×10^{-5}	b	473				[84]
Co$_2$(TTFTB)	1.49×10^{-5}	b	531				[84]
Zn$_2$(TTFTB)	3.95×10^{-6}	b	535			1.75	[84]
Cd$_2$(TTFTB)	2.86×10^{-4}	b	460			1.75	[84]
Sr(Hbtd)(H$_2$O)	6.5×10^{-6}	a			2.04	2.3	[85]
NNU-27	1.3×10^{-3}	b					[86]
K$_{(0-2)}$Fe$_2$(BDP)$_3$	10^{-7}–10^{-2}	b, e	430–1230			0.5–1.49	[79]
Fe$_2$(BDT)$_3$	6×10^{-5}	b	614		2	2	[80]
Fe$_2$(BDT)$_3$	1.8(oxidized)	b				1.4	[80]
PMC-1	1.5–7.6×10^{-6}	a					[87]
PMC-1	1.0~3.0×10^{-3}	b					[87]
Fe-THQ	3.3×10^{-3}	e	~163		0	0.79	[88]
Zn-HAB	8.6×10^{-4}	e	~145	~20		1.82	[89]
Eu$_6$HOTP$_2$	1.48×10^{-6}	a					[90]
Y$_6$HOTP$_2$	2.0×10^{-5}	a	780				[90]
Nd-HHTP	8.0×10^{-4}	a	513	~16	0	0.82	[36b]
Ho-HHTP	5.3×10^{-5}	a	208	~16	0	0.76	[36b]
Yd-HHTP	1×10^{-5}	a	452	~16	0	0.73	[36b]
La-HHTP	8.2×10^{-4}	a	325	~16	0	0.85	[36b]
Zn-NDI-A	2×10^{-7}	a			1.6		[91]
Fe-THBQ	2.7×10^{-4}	e	7.88			0.63	[92]
Co-THBQ	6×10^{-8}	e	42.86			1.44	[92]
Mn-THBQ	3.5×10^{-8}	d	36.5			1.69	[92]
Fe-HHTP	5.6×10^{-3}	f	1490	17.8		1.09	[71]
TUB40	2	a			2.195	1.42	[93]
GTUB3	4×10^{-2}	b	671	4–6		1.64	[94]
Ni-3D($-$ox)	2.9×10^{-5}	e	120			1.6	[60]
Cu-THQ-BPY	2.2×10^{-8}	e	196.9	~7.3, 14		1.01	[35]
Nd$_{1.5}$HOTP	1.08×10^{3}	e			0		[95]
La$_{1.5}$HOTP	9×10^{2}	e			0		[95]
Cu-TAPT	4.04	b	41.5		0	0.9	[81]
Cu-TAPT	0.11	a	41.5		0	0.9	[81]
Fe$_2$(dhbq)$_3$	1.2×10^{-2}	e	556	4.6			[82]
Spiro-CS$_2$Ni	1.1×10^{-7}	c	400	~15			[96]
d-HBC-12O-Cu	3.31×10^{-2}	a	116			1.48	[97]

a: two-probe pellet; b: two-probe crystal; c: two-probe film; d: four-probe pellet; e: four-probe crystal; f: Van der Pauw pellet.

states (originating from the ligand), with the charge and discharge processes accompanying cation and anion insertion/desertion. Based on this principle, NiDI, when used as lithium-ion cathode materials, achieved a significant specific capacity of 155 mAh g^{-1}, comparable to commercial lithium battery cathode materials, as well as 300 stable cycles. In contrast to the aforementioned redox activity solely originating from organic ligands, Jiang et al.[99] found that when Cu-THQ is used as lithium-ion battery cathode materials, both Cu^{2+} and the organic ligand exhibit noticeable redox activity during the charge and discharge process. Therefore, it exhibits an ultra-high specific capacity of 387 mAh g^{-1} and good cycling stability,

Batteries & Supercaps

Review
doi.org/10.1002/batt.202300536

Chemistry
Europe

European Chemical
Societies Publishing

retaining 340 mAh g^{-1} after 100 cycles. This study provides an effective strategy for the rational design and development of next-generation lithium-ion battery cathode materials based on 2D c-MOFs.

At the same time, Wu et al.[100] investigated the application of a highly conductive MOF, Cu-BHT, as cathode materials in lithium-ion batteries (LIBs). Density Functional Theory (DFT) calculations were utilized to calculate the Density of States (DOS) at different ring positions of Cu-BHT (benzenehexathiolate) with Li$^+$ insertion. The original Cu-BHT already had a small band gap, indicating its inherent high conductivity. When Li$^+$ was loaded in a 6-membered or carbon ring, the new electronic state was prominently shown. The increased electronic conductivity indicates that Cu-BHT has excellent reversibility and outstanding lithium storage as cathode materials for LIBs. Furthermore, the Li-ion diffusion barrier of Cu-BHT was lower than that of typical LIBs electrode materials, indicating that Cu-BHT holds significant promise for achieving fast Li-ion diffusion performance.

In addition to the redox activity of electrode materials affecting energy storage performance, recent work has pointed out that the particle morphology of 2D c-MOFs significantly impacts the electrochemical lithium-ion storage kinetics. Rod-like and flake-like Cu$_3$(HHTP)$_2$ c-MOFs were obtained by adjusting the proportions of reactants and the types of additives.[101] Due to the larger external surface area and shorter ion diffusion paths, plate-shaped particles demonstrated higher kinetics and negligible diffusion limitation compared to rod-like particles. It paves the way for the optimization of redox-active porous structures to overcome diffusion limitations in the Faraday process.

Current applications of c-MOFs in Li-S batteries can be divided into two aspects, modifying the separator and mixing with sulfur for use as electrode materials. A representative work reported the modification of a separator using c-MOFs.[102] Ni-TABQ and Ni-BTC grew on a polypropylene (PP) separator by interface growth, forming a MOF film about 1.8 μm thick. The capturing ability of Ni-MOFs for soluble lithium polysulfides (LiPSs) was studied by DFT, and the results suggested that both Ni-TABQ and Ni-BTC could capture LiPSs via chemical interactions, effectively lowering the energy barrier for sulfur materials during redox reactions. With the synergistic effect of the quinone and Ni-N$_4$ chemical group dual catalytic sites, Ni-TABQ showed more potential. Ultimately, because the MOF film can simultaneously achieve ion sieving, LiPSs adsorption, and multi-step catalytic conversion (Figure 6(A and B)), the Li-S battery assembled with a Ni-TABQ-modified separator exhibited an ultra-low capacity decay rate of 0.0198% over 1000 cycles at 1 C and an ultra-high capacity of 5.59 mAh cm^{-2} after 100 cycles under high sulfur loading and lean electrolyte conditions.

ZnCo-based conductive bimetallic MOF nanoboxes were prepared through continuous metal ion and ligand exchange and successfully used as sulfur hosts in lithium-sulfur (Li-S) batteries.[103] Due to the presence of Co-O$_4$ groups, ZnCo-MOF can effectively adsorb LiPSs, thereby promoting the redox kinetics of LiPSs and suppressing the shuttle effect. Additionally, the hollow nanostructure provides enough internal space for

high sulfur loading and accommodates the large volume expansion of sulfur. Therefore, the assembled Li-S battery displayed an ultra-high reversible capacity of 1076 mAh g^{-1} at a current density of 0.1 C and over 300 cycles at 0.5 C, with a capacity decay rate of 0.048% per cycle. On the other hand, the application of Cu-BHT in Li-S batteries was studied from the perspective of DFT simulation.[104] The binding energy of S$_8$ and Li$_2$S$_n$ on a single layer of Cu-BHT DFT was calculated. The results revealed that S$_8$ exhibited the lowest binding energy, while the binding energy increased with the increase in n for Li$_2$S$_n$. Furthermore, the binding energy of long-chain Li$_2$S$_n$ molecules with the Cu-BHT monolayer was found to be greater than that with the electrolyte solvents 1,2-dimethoxyethane (DME) and 1,3-dioxolane (DOL). That suggests that polysulfide lithium molecules tend to anchor onto the Cu-BHT monolayer rather than dissolve in the electrolyte. Moreover, this adsorption energy is higher than other S host materials, making it a promising anchoring materials.

Li-O$_2$ batteries still face the challenges of slow electrode reaction kinetics and large overpotential due to Li$_2$O$_2$.[105] In recent years, researchers have tried to use c-MOFs to solve these problems.[106] In 2021, Chen and co-workers adopted a photocatalytic strategy, using Co-TABQ c-MOF as a bifunctional catalyst to promote the kinetics of the cathode reaction. During the discharge process, O$_2$ is first adsorbed on the Co atoms of Co-TABQ and accepts electrons under illumination from the d$_z^2$ and d$_{xz}$ orbitals of Co atoms in the π_{2p}^* orbitals, which facilitates reduction to LiO$_2$, then further reduced to Li$_2$O$_2$. During the charging process, the holes generated in the d$_z^2$ orbitals of Co are mobilized under the action of the applied voltage, enabling the fast decomposition of Li$_2$O$_2$ to O$_2$ and Li$^+$. This resulted in discharge and charge voltages of 3.12 V and 3.32 V, respectively, and a round-trip efficiency of 94.0%.[106]

In addition, Furthermore, efforts have been made by researchers to enhance the energy storage performance of Li-O$_2$ batteries through the modification of the growth state of Li$_2$O$_2$. Majidi et al.[105] embedded Ru atoms into the Ni-HTP (2,3,6,7,10,11-hexaiminotriphenylene) framework to obtain the NiRu-HTP bimetallic c-MOF. The presence of Ru-N$_4$ sites led to the formation of a thin film of Li$_2$O$_2$ on the surface of NiRu-HTP, promoting electron transfer and ion diffusion at the electrode-electrolyte interface and the reversible decomposition of Li$_2$O$_2$ during the discharge process. As a result, a Li-O$_2$ battery with NiRu-HTP as the cathode exhibited a reduced charge/discharge polarization of 0.76 V and excellent cycle stability (200 cycles without performance decay). Similarly, when Cu-THQ was used as the cathode materials, it promoted the growth of nanocrystalline Li$_2$O$_2$ in the amorphous region.[107] The encapsulation of 2–5 nm Li$_2$O$_2$ crystals in the amorphous Li$_2$O$_2$ was revealed by TEM. Because of the inherent conductivity of the Li$_2$O$_2$ crystals, this structure was proven to effectively reduce the charge potential.

Given the resource constraints and safety issues associated with lithium metal, non-lithium-ion-based battery systems, such as sodium-ion batteries, potassium-ion batteries, and zinc-ion batteries, have been the focus of researchers as potential future alternatives.[32,108] For example, in 2019, Stoddart's group[108a]
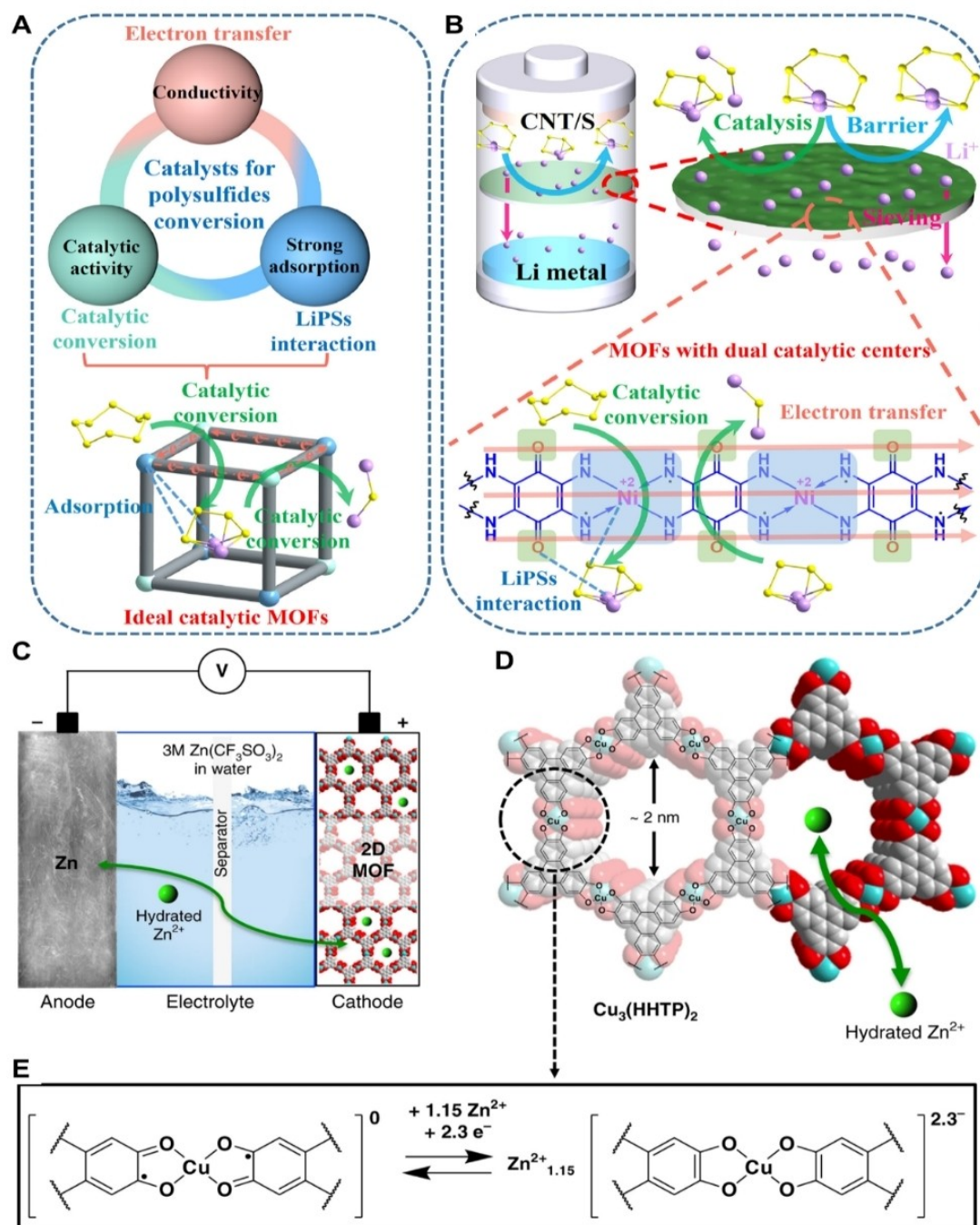
Batteries & Supercaps

Review
doi.org/10.1002/batt.202300536

Chemistry Europe
European Chemical
Societies Publishing

Figure 6. c-MOFs-based batteries. (A and B) Goal-directed design of MOF and its membrane for suppressing shuttle effect in LSBs.[102] Copyright 2022 Elsevier. (A) Illustration of key elements in ideal catalytic MOFs for high-performance LSBs. (B) The design philosophy of catalytic MOF interlayer for the ions sieving and multistep catalytic conversion of LiPSs. (C) Schematic illustration of the rechargeable Zn-2D MOF cell. (D) Structure of $Cu_3(HHTP)_2$, which when viewed down the c axis, exhibits slipped-parallel stacking of 2D sheets with a honeycomb lattice. The cyan, red, and gray spheres represent Cu, O, and C atoms, respectively. The H atoms are omitted for the sake of clarity. (E) Expected redox process in the coordination unit of $Cu_3(HHTP)_2$.[108a] (C–E) Copyright 2019 The Author(s). Published by Springer Nature.

successfully applied Cu-HHTP c-MOF to zinc-ion batteries, achieving a high reversible capacity of 228 mAh g^{-1} under 50 mV s^{-1}. This was the first successful application of c-MOF in aqueous zinc-ion batteries, and it also exhibited the highest capacity among open pore structures used as cathodes, including Prussian Blue analogs. During the charging process, Zn^{2+} are stored in the pores, and during the discharge process,

they are expelled and do not damage the c-MOF structure (Figure 6(C–E)). Further, by conducting linear cyclic voltammetry tests at different scan speeds and combining them with the power law equation, the pseudocapacitive intercalation charge storage mechanism of Cu-HHTP MOF is determined. Thus, the advantages of batteries (high capacitance) and supercapacitors (high rate) were successfully integrated into one system. More

Batteries & Supercaps

Review
doi.org/10.1002/batt.202300536

**Chemistry
Europe**
European Chemical
Societies Publishing

Table 2. Performance of c-MOFs in batteries.

Name of c-MOFs	Role	Battery type (voltage (V))	Low-rate capacity (mAh g^{-1}) (current (mA g^{-1}))	Reversible capacity (mAh g^{-1}) (current (mA g^{-1}), cycle number, capacity retention)	Ref.
Fe(dhbq)	cathode	Li-ion (1.5–4.0)	264 (28)		[109]
Cu-BHT	cathode	Li-ion (1.5–3.0)	232 (50)	175 (300, 500, 92.4%)	[110]
Ni-DI	cathode	Li-ion (2.0–4.5)	155 (10)	~50 (250, 300)	[98]
Cu$_3$(HHTP)$_2$	cathode	Li-ion (1.7–3.5)	100 (100)	~74 (100, 100)	[101]
Cu-HHTQ	anode	Li-ion (0.01–3.0)	989 (15)	657.6 (600, 200, 82%)	[111]
Fe-TTTP	anode	Li-ion (0.01–3.0)	950 (50)	310 (2000, 5000 E)	[112]
Cu-CAT	anode	Li-ion (0.01–3.0)	631 (200)	540 (500, 500, 81%)	[113]
Ni$_3$(HITP)$_2$	anode	Li-ion (0.01–3.0)	1078 (100)	578 (2000, 500, 63%)	[114]
Co-Ni-BTC	anode	Li-ion (0.005–3.0)	1210 (100)	1051 (100, 300, 86.7%)	[115]
Cu$_3$(HHTP)$_2$	cathode	Li-ion (1.7–3.5)	105 (1 C)	42 (20 C, 500, 88.5%)	[116]
Co-BTC	anode	Li-ion (0.01–3.0)	845 (100)	473 (2000, 500)	[117]
Ni-HITP	anode	Li-ion (0.01–3.0)	1280 (100)	392 (1000, 1000)	[118]
Cu-THQ	cathode	Li-ion (1.2–4.0)	387 (50)	340 (50, 100, 85%)	[99]
HHB-Cu NSs	cathode	Li-ion (1.3–2.6)	153 (100)	~89 (1000, 1000, 90%)	[119]
CuPcOH	cathode	Li-ion (2.0–4.4)	193 (50)	~50 (130, 200)	[120]
Ni-TIB	anode	Li-ion (0.8–2.0)	200 (20000)	83 (20000, 20000, 79%)	[121]
Cu-TIB	cathode	Li-ion (1.5–4.1)	262 (50)		[121]
Fe$_2$(dhbq)$_3$	cathode	Li-ion (1.3–4.0)	322 (41)		[82]
CoDI	cathode	Li-ion (1.0–3.5)	221 (100)		[122]
NiDI	cathode	Li-ion (1.0–3.5)	156 (100)		[122]
Co$_x$Ni$_{1-x}$DI	cathode	Li-ion (1.0–3.5)	248 (100)	200 (100, 20)	[122]
(H$_2$NMe$_2$)$_2$Fe$_2$(Cl$_2$dhbq)$_3$	cathode	Li-ion (1.8–4.2)	195 (20)	104 (40, 50)	[123]
Ni-S	anode	Li-ion (0.005–3.0)	1164 (100)	705 (100, 180)	[124]
Ni-NH	anode	Li-ion (0.005–3.0)	1195 (100)	273 (100, 180)	[124]
(NBu$_4$)$_2$Fe$_2$(DHBQ)$_3$	cathode	Li-ion (1.5–3.5)	137.2 (10)	103.1 (500, 350, 91.4%)	[125]
Ni$_3$(HITP)$_2$	separator	Li-S (1.8–3.0)	1220.1 (0.1 C)	~600 (0.5 C, 200, ~60%)	[126]
Co$_3$(HITP)$_2$	separator	Li-S (1.7–2.8)	912 (0.5 C)	454 (1 C, 1000, 72%)	[69a]
Ni$_3$(HITP)$_2$	separator	Li-S (1.7–2.8)	1186 (0.2 C)	716 (1 C, 500, 81.4%)	[127]
ZnCo-MOF NBs	cathode	Li-S (1.7–2.8)	1076 (0.2 C)	668 (1 C, 300, 93.1%)	[103]
Ni-TABQ	separator	Li-S (1.7–2.8)	1497 (0.1 C)	1023 (1 C 1000, 80.2%)	[102]
Ni$_3$(HITP)$_2$	cathode	Li-S (1.7–2.8)	208 (300)	125 (2500, 3200, 95%)	[128]
NiRu-HTP	cathode	Li-O$_2$			[105]
Co-TABQ	cathode	Li-O$_2$			[106]
Cu-THQ	cathode	Li-O$_2$			[107]
P(THBQ-Al)	cathode	Na-ion (1.5–3.0)	113 (20)		[129]
Fe$_2$-O$_8$-PcCu	cathode	Na-I$_2$ (2.0–3.4)	208 (1300)	150 (1500 3200, 95%)	[130]
HATN-SCu	anode	Na-ion (0.01–3.0)	231 (100)	88 (2000, 1000, 100%)	[131]
HATN-OCu	anode	Na-ion (0.01–3.0)	500 (100)	152 (2000, 1000, 58%)	[131]
1D-CuTABQ	cathode	Na-ion (1.0–3.8)	328.6 (100)	320 (1000, 300, 80%)	[132]
2D-CuTABQ	cathode	Na-ion (1.0–3.8)	305 (100)	220 (1000, 300, 63%)	[132]
Zn-HHTP	cathode	Na-ion (1.0–3.5)	~150 (100)	~135 (1000, 5000, 70%)	[133]
Cu-HHTP	cathode	Na-ion (1.0–3.5)	~200 (100)	~100 (1000, 600)	[133]
Ni-TABQ	anode	Na-ion (0.2–3.0)	469 (100)	~330 (2000, 450, 88.5%)	[134]
Ni-BTA	anode	Na-ion (0.01–2.5)	~500 (100)	~290 (1000, 1000)	[61]
Cu-TCNQ	cathode	Na-ion (2.0–4.1)	255 (20)	214 (50, 50)	[135]
Ni-TIB	anode	K-ion (0.5–2.0)	220 (100)	~200 (1000, 200, 95.6%)	[108b]
Ni-ETT	cathode	Na-ion (1.2–3.2)	155 (100)	137 (1000, 1000, 76%)	[136]

Table 2. continued					
Name of c-MOFs	Role	Battery type (voltage (V))	Low-rate capacity (mAh g^{-1}) (current (mA g^{-1}))	Reversible capacity (mAh g^{-1}) (current (mA g^{-1}), cycle number, capacity retention)	Ref.
Cu-CAT	anode	Na-ion (0.01–2.4)	~260 (100)	~221 (100, 200, 85%)	[137]
Mn/Fe-HIB	cathode	Zn-air			[138]
Cu-TAPT	cathode	Na-ion (1.0–3.8)	313.4 (100)	~152 (5000, 1500, 77%)	[81]
Co-HAB	cathode	Na-ion (0.5–3.0)	295 (50)	152 (12000)	[32]
Cu$_3$(HHTP)$_2$	cathode	Zn-ion (0.5–1.3)	228 (50)	152.4 (500, 100, 75%)	[108a]
Ni-DAB	anode	K-ion (0.4–2.0)	183 (50)	158 (1000, 600, 91.4%)	[139]

specific information about the capacities and voltage windows of battery systems based on c-MOFs can be found in Table 2.

4. Summary and outlook

In this review, we have elucidated the influential factors governing the synthesis of c-MOFs and explored their applications in various electrochemical energy storage devices, including supercapacitors, LIBs, zinc-ion batteries, and so on. However, amid the remarkable progress in the field of c-MOFs, we acknowledge the critical challenges that demand attention. The bottlenecks and prospects in the field of c-MOFs are present as follows:

1) While there has been a substantial amount of work related to c-MOFs, most of these studies mainly report on the materials' synthesis and applications, rarely touching on the crystallization process of c-MOFs. The research into the crystallization process of c-MOFs is crucial for determining the specific mechanisms of reaction conditions, decoupling the relationship between reaction conditions and c-MOFs products (a significant challenge in the entire field of MOFs synthesis currently),[21] and it is extremely key to the synthesis of high-crystallinity c-MOFs.

2) The synthesis of c-MOFs often results in materials with relatively low crystallinity and inadequate activation, limiting their applications significantly. For example, low crystallinity often results in a lower specific surface area than the theoretical value, which in the case of supercapacitors leads to fewer ion adsorption sites and a decrease in capacitance.[19] Furthermore, most c-MOFs obtained in experiments are in the form of powders, making it difficult to produce large single crystals, hindering the determination of the structure of c-MOFs and the investigation of their conductivity mechanisms.[26] The preparation of large single crystals is crucial for a deep understanding of conductivity mechanisms and the design and development of new c-MOFs.

3) Most existing c-MOFs have a 2D stacking structure.[140] Although 3D c-MOFs have been receiving increasing attention in recent years, their overall number is still small. Meanwhile, there are uncertainties about their conduction mechanisms. In comparison with 2D c-MOFs, 3D c-MOFs have a larger specific surface area, more active sites, and a more developed pore structure.[71] Therefore, their applications in the field of energy storage are highly promising.

4) Due to the well-defined crystalline structure of c-MOFs, computational tools, such as DFT and MD, are playing an increasingly significant role in the determination of c-MOF structures, the investigation of conduction mechanisms, and the study of energy storage mechanisms. Additionally, the emergence of ML has provided a new approach for the high-throughput screening and prediction of new c-MOFs.[141]

5) The current synthesis cost of c-MOFs is considerably high, primarily due to the exorbitant prices of organic linkers such as tetrathiafulvalene and triphenylene-based organic linkers.[142] This significantly restricts the practical application of c-MOFs. In the future, efforts are required to intensify research on the synthesis of organic linkers to reduce costs, making the practical application of c-MOFs.

In conclusion, although the development of c-MOFs still faces many challenges, they are receiving increasing attention and have made rapid progress. We believe in the enormous potential of c-MOFs in the field of electrochemical energy storage and hope that this review could provide some assistance and insights for researchers in their future studies on c-MOFs.

Conflict of Interests

The authors have no conflicts to disclose.

Batteries & Supercaps

Review

doi.org/10.1002/batt.202300536

Chemistry
Europe

European Chemical
Societies Publishing

[1] a) B. Dunn, H. Kamath, J.-M. Tarascon, *Science* **2011**, *334*, 928; b) C.-Y. Wang, T. Liu, X.-G. Yang, S. Ge, N. V. Stanley, E. S. Rountree, Y. Leng, B. D. McCarthy, *Nature* **2022**, *611*, 485.

[2] a) T. Mo, Z. Wang, L. Zeng, M. Chen, A. A. Kornyshev, M. Zhang, Y. Zhao, G. Feng, *Adv. Mater.* **2023**, *35*, 2301118; b) Z. Xiao, S. Wang, X. Yan, C. Liu, X. Zhao, X. Yang, *Batteries & Supercaps* **2019**, *2*, 766; c) K. Wang, C. Chen, Y. Li, Y. Hong, H. Wu, C. Zhang, Q. Zhang, *Small* **2023**, *19*, 2300054; d) Y. Rudel, M. Rana, J. Ruhl, C. Rosenbach, J. Müller, P. Michalowski, A. Kwade, W. G. Zeier, *Batteries & Supercaps* **2023**, *6*, e202300211.

[3] a) Y. Zhu, S. Murali, M. D. Stoller, K. J. Ganesh, W. Cai, P. J. Ferreira, A. Pirkle, R. M. Wallace, K. A. Cychosz, M. Thommes, D. Su, E. A. Stach, R. S. Ruoff, *Science* **2011**, *332*, 1537; b) J. Li, N. Sharma, Z. Jiang, Y. Yang, F. Monaco, Z. Xu, D. Hou, D. Ratner, P. Pianetta, P. Cloetens, F. Lin, K. Zhao, Y. Liu, *Science* **2022**, *376*, 517.

[4] G. Wang, L. Zhang, J. Zhang, *Chem. Soc. Rev.* **2012**, *41*, 797.

[5] H. Shao, Y.-C. Wu, Z. Lin, P.-L. Taberna, P. Simon, *Chem. Soc. Rev.* **2020**, *49*, 3005.

[6] B. P. Block, S. H. Rose, C. W. Schaumann, E. S. Roth, J. Simkin, *J. Am. Chem. Soc.* **1962**, *84*, 3200.

[7] S. Kitagawa, S. Kawata, Y. Nozaka, M. Munakata, *J. Chem. Soc. Dalton Trans.* **1993**, *9*, 1399.

[8] B. F. Hoskins, R. Robson, *J. Am. Chem. Soc.* **1990**, *112*, 1546.

[9] H. Li, M. Eddaoudi, M. O'Keeffe, O. M. Yaghi, *Nature* **1999**, *402*, 276.

[10] D. Riou, G. Férey, *J. Mater. Chem.* **1998**, *8*, 2733.

[11] a) E. J. Carrington, C. A. McAnally, A. J. Fletcher, S. P. Thompson, M. Warren, L. Brammer, *Nat. Chem.* **2017**, *9*, 882; b) J. Li, X. Han, X. Zhang, A. M. Sheveleva, Y. Cheng, F. Tuna, E. J. L. McInnes, L. J. McCormick Mcpherson, S. J. Teat, L. L. Daemen, A. J. Ramirez-Cuesta, M. Schröder, S. Yang, *Nat. Chem.* **2019**, *11*, 1085; c) P. G. Boyd, A. Chidambaram, E. García-Díez, C. P. Ireland, T. D. Daff, R. Bounds, A. Gładysiak, P. Schouwink, S. M. Moosavi, M. M. Maroto-Valer, J. A. Reimer, J. A. R. Navarro, T. K. Woo, S. Garcia, K. C. Stylianou, B. Smit, *Nature* **2019**, *576*, 253; d) Y. Zhong, X. Su, W. Wang, Z. Shao, *Batteries & Supercaps* **2019**, *2*, 272; e) W. Li, C. Wu, H. Ren, W. Fang, L. Zhao, K. N. Dinh, *Batteries & Supercaps* **2020**, *3*, 1321.

[12] a) D. Sheberla, J. C. Bachman, J. S. Elias, C.-J. Sun, M. Dincă, *Nat. Mater.* **2017**, *16*, 220; b) D. Feng, T. Lei, M. R. Lukatskaya, J. Park, Z. Huang, M. Lee, L. Shaw, S. Chen, A. A. Yakovenko, A. J. N. E. Kulkarni, *Nat. Energy* **2018**, *3*, 30.

[13] L. S. Xie, G. Skorupskii, M. Dincă, *Chem. Rev.* **2020**, *120*, 8536.

[14] L. Sarkisov, *Adv. Mater.* **2012**, *24*, 3130.

[15] O. K. Farha, A. Özgür Yazaydın, I. Eryazici, C. D. Malliakas, B. G. Hauser, M. G. Kanatzidis, S. T. Nguyen, R. Q. Snurr, J. T. Hupp, *Nat. Chem.* **2010**, *2*, 944.

[16] a) G. Chen, Z. Li, Z. Huang, H. Lu, G. Long, J. S. Lezama Pacheco, J. B. H. Tok, T. Z. Gao, Y. Lei, J. Zhou, Z. Bao, *ACS Nano* **2023**, *17*, 9611; b) L. Sun, B. Liao, D. Sheberla, D. Kraemer, J. Zhou, E. A. Stach, D. Zakharov, V. Stavila, A. A. Talin, Y. Ge, M. D. Allendorf, G. Chen, F. Léonard, M. Dincă, *Joule* **2017**, *1*, 168; c) P. Zhang, M. Wang, Y. Liu, S. Yang, F. Wang, Y. Li, G. Chen, Z. Li, G. Wang, M. Zhu, R. Dong, M. Yu, O. G. Schmidt, X. Feng, *J. Am. Chem. Soc.* **2021**, *143*, 10168.

[17] L. S. Xie, G. Skorupskii, M. Dinca, *Chem. Rev.* **2020**, *120*, 8536.

[18] T. Düren, F. Millange, G. Férey, K. S. Walton, R. Q. Snurr, *J. Phys. Chem. C* **2007**, *111*, 15350.

[19] S. Bi, H. Banda, M. Chen, L. Niu, M. Chen, T. Wu, J. Wang, R. Wang, J. Feng, T. Chen, M. Dinca, A. A. Kornyshev, G. Feng, *Nat. Mater.* **2020**, *19*, 552.

[20] a) N. Contreras-Pereda, S. Pané, J. Puigmartí-Luis, D. Ruiz-Molina, *Coord. Chem. Rev.* **2022**, *460*, 214459; b) W.-H. Li, W.-H. Deng, G.-E. Wang, G. Xu, *EnergyChem* **2020**, *2*, 100029; c) L. Sun, M. G. Campbell, M. Dinca, *Angew. Chem. Int. Ed.* **2016**, *55*, 3566; d) K. Fan, C. Zhang, Y. Chen, Y. Wu, C. Wang, *Chem* **2021**, *7*, 1224; e) C. Li, L. Zhang, J. Chen, X. Li, J. Sun, J. Zhu, X. Wang, Y. Fu, *Nanoscale* **2021**, *13*, 485.

[21] O. M. Yaghi, *Chem* **2022**, *8*, 1541.

[22] A. K. Cheetham, G. Kieslich, H. H. M. Yeung, *Acc. Chem. Res.* **2018**, *51*, 659.

[23] S. Jung, M. Oh, *Angew. Chem. Int. Ed.* **2008**, *47*, 2049.

[24] M. Dan, C. N. R. Rao, *Angew. Chem. Int. Ed.* **2006**, *45*, 281.

[25] C. Gerardin, M. In, L. Allouche, M. Haouas, F. Taulelle, *Chem. Mater.* **1999**, *11*, 1285.

[26] J.-H. Dou, M. Q. Arguilla, Y. Luo, J. Li, W. Zhang, L. Sun, J. L. Mancuso, L. Yang, T. Chen, L. R. Parent, G. Skorupskii, N. J. Libretto, C. Sun, M. C. Yang, P. V. Dip, E. J. Brignole, J. T. Miller, J. Kong, C. H. Hendon, J. Sun, M. Dincă, *Nat. Mater.* **2021**, *20*, 222.

[27] H. Wei, Y. Tian, Q. Chen, D. Estevez, P. Xu, H.-X. Peng, F. Qin, *Chem. Eng. J.* **2021**, *405*, 126637.

[28] H. T. B. Pham, J. Y. Choi, S. Huang, X. Wang, A. Claman, M. Stodolka, S. Yazdi, S. Sharma, W. Zhang, J. Park, *J. Am. Chem. Soc.* **2022**, *144*, 10615.

[29] N. T. T. Nguyen, H. Furukawa, F. Gándara, C. A. Trickett, H. M. Jeong, K. E. Cordova, O. M. Yaghi, *J. Am. Chem. Soc.* **2015**, *137*, 15394.

[30] X. Cheng, A. Zhang, K. Hou, M. Liu, Y. Wang, C. Song, G. Zhang, X. Guo, *Dalton Trans.* **2013**, *42*, 13698.

[31] T. Chalati, P. Horcajada, R. Gref, P. Couvreur, C. Serre, *J. Mater. Chem. A* **2011**, *21*, 2220.

[32] J. Park, M. Lee, D. Feng, Z. Huang, A. C. Hinckley, A. Yakovenko, X. Zou, Y. Cui, Z. Bao, *J. Am. Chem. Soc.* **2018**, *140*, 10315.

[33] a) D. Sheberla, L. Sun, M. A. Blood-Forsythe, S. Er, C. R. Wade, C. K. Brozek, A. Aspuru-Guzik, M. Dinca, *J. Am. Chem. Soc.* **2014**, *136*, 8859; b) R. W. Day, D. K. Bediako, M. Rezaee, L. R. Parent, G. Skorupskii, M. Q. Arguilla, C. H. Hendon, I. Stassen, N. C. Gianneschi, P. Kim, M. Dinca, *ACS Cent. Sci.* **2019**, *5*, 1959.

[34] L. S. Xie, E. V. Alexandrov, G. Skorupskii, D. M. Proserpio, M. Dincă, *Chem. Sci.* **2019**, *10*, 8558.

[35] J. Y. Choi, J. Flood, M. Stodolka, H. T. B. Pham, J. Park, *ACS Nano* **2022**, *16*, 3145.

[36] a) D. G. Ha, M. Rezaee, Y. Han, S. A. Siddiqui, R. W. Day, L. S. Xie, B. J. Modtland, D. A. Muller, J. Kong, P. Kim, M. Dinca, M. A. Baldo, *ACS Cent. Sci.* **2021**, *7*, 104; b) G. Skorupskii, B. A. Trump, T. W. Kasel, C. M. Brown, C. H. Hendon, M. Dincă, *Nat. Chem.* **2020**, *12*, 131.

[37] A. K. Cheetham, C. N. R. Rao, R. K. Feller, *Chem. Commun.* **2006**, *2006*, 4780.

[38] E. Haque, S. H. Jhung, *Chem. Eng. J.* **2011**, *173*, 866.

[39] D. J. Tranchemontagne, J. R. Hunt, O. M. Yaghi, *Tetrahedron* **2008**, *64*, 8553.

[40] E. Biemmi, S. Christian, N. Stock, T. Bein, *Microporous Mesoporous Mater.* **2009**, *117*, 111.

[41] a) S. Shankar, R. Balgley, M. Lahav, S. R. Cohen, R. Popovitz-Biro, M. E. Van Der Boom, *J. Am. Chem. Soc.* **2015**, *137*, 226; b) S. Bauer, T. Bein, N. Stock, *Inorg. Chem.* **2005**, *44*, 5882.

[42] D. Feng, T. Lei, M. R. Lukatskaya, J. Park, Z. Huang, M. Lee, L. Shaw, S. Chen, A. A. Yakovenko, A. Kulkarni, J. Xiao, K. Fredrickson, J. B. Tok, X. Zou, Y. Cui, Z. Bao, *Nat. Energy* **2018**, *3*, 30.

[43] a) M. Hmadeh, Z. Lu, Z. Liu, F. Gándara, H. Furukawa, S. Wan, V. Augustyn, R. Chang, L. Liao, F. Zhou, E. Perre, V. Ozolins, K. Suenaga, X. Duan, B. Dunn, Y. Yamamto, O. Terasaki, O. M. Yaghi, *Chem. Mater.* **2012**, *24*, 3511; b) M. Stodolka, J. Y. Choi, J. Flood, H. T. B. Pham, J. Park, *ACS Applied Nano Materials* **2022**, *5*, 2156.

[44] T. Chen, J. H. Dou, L. Yang, C. Sun, N. J. Libretto, G. Skorupskii, J. T. Miller, M. Dinca, *J. Am. Chem. Soc.* **2020**, *142*, 12367.

[45] a) J. Lv, W. Li, J. Li, Z. Zhu, A. Dong, H. Lv, P. Li, B. Wang, *Angew. Chem. Int. Ed.* **2023**, *135*; b) Y. Zhao, J. Wang, R. Pei, *J. Am. Chem. Soc.* **2020**, *142*, 10331; c) C. R. Marshall, J. P. Dvorak, L. P. Twight, L. Chen, K. Kadota, A. B. Andreeva, A. E. Overland, T. Ericson, A. F. Cozzolino, C. K. Brozek, *J. Am. Chem. Soc.* **2022**, *144*, 5784.

[46] B. Seoane, S. Castellanos, A. Dikhtiarenko, F. Kapteijn, J. Gascon, *Coord. Chem. Rev.* **2016**, *307*, 147.

[47] J. M. Chin, E. Y. Chen, A. G. Menon, H. Y. Tan, A. T. S. Hor, M. K. Schreyer, J. Xu, *CrystEngComm* **2013**, *15*, 654.

[48] A. Schaate, P. Roy, A. Godt, J. Lippke, F. Waltz, M. Wiebcke, P. Behrens, *Chem. Eur. J.* **2011**, *17*, 6643.

[49] J. W. Gittins, C. J. Balhatchet, S. M. Fairclough, A. C. Forse, *Chem. Sci.* **2022**, *13*, 9210.

[50] B. Hoppe, K. D. J. Hindricks, D. P. Warwas, H. A. Schulze, A. Mohmeyer, T. J. Pinkvos, S. Zailskas, M. R. Krey, C. Belke, S. König, M. Fröba, R. J. Haug, P. Behrens, *CrystEngComm* **2018**, *20*, 6458.

[51] S. Shang, C. Du, Y. Liu, M. Liu, X. Wang, W. Gao, Y. Zou, J. Dong, Y. Liu, J. Chen, *Nat. Commun.* **2022**, *13*, 7599.

[52] T. M. Tovar, J. Zhao, W. T. Nunn, H. F. Barton, G. W. Peterson, G. N. Parsons, M. D. LeVan, *J. Am. Chem. Soc.* **2016**, *138*, 11449.

[53] J. Y. Choi, M. Wang, B. Check, M. Stodolka, K. Tayman, S. Sharma, J. Park, *Small* **2023**, *19*, 2206988.

[54] a) Z. Chang, M. Zhu, Y. Sun, F. He, Y. Li, C. Ye, Y. Jin, Z. Li, W. Xu, *Adv. Funct. Mater.* **2023**, *33*, 2301513; b) M. Wang, H. Shi, P. Zhang, Z. Liao, M. Wang, H. Zhong, F. Schwotzer, A. S. Na, E. Zschech, S. Zhou, S. Kaskel, R. Dong, X. Feng, *Adv. Funct. Mater.* **2020**, *30*, 2002664.

[55] E. Haque, N. A. Khan, J. H. Park, S. H. Jhung, *Chemistry – A European Journal* **2010**, *16*, 1046.

[56] Y. Liu, Y. Wei, M. Liu, Y. Bai, X. Wang, S. Shang, J. Chen, Y. Liu, *Angew. Chem. Int. Ed.* **2021**, *60*, 2887.

Batteries & Supercaps

Review

doi.org/10.1002/batt.202300536

Chemistry
Europe

European Chemical
Societies Publishing

[57] N. Stock, S. Biswas, *Chem. Rev.* **2012**, *112*, 933.

[58] J. H. Bang, K. S. Suslick, *Adv. Mater.* **2010**, *22*, 1039.

[59] J.-H. Dou, L. Sun, Y. Ge, W. Li, C. H. Hendon, J. Li, S. Gul, J. Yano, E. A. Stach, M. Dincă, *J. Am. Chem. Soc.* **2017**, *139*, 13608.

[60] T. Chen, J.-H. Dou, L. Yang, C. Sun, J. J. Oppenheim, J. Li, M. Dincă, *J. Am. Chem. Soc.* **2022**, *144*, 5583.

[61] Y. Chen, M. Tang, Y. Wu, X. Su, X. Li, S. Xu, S. Zhuo, J. Ma, D. Yuan, C. Wang, W. Hu, *Angew. Chem. Int. Ed.* **2019**, *58*, 14731.

[62] a) M. D. Allendorf, R. Dong, X. Feng, S. Kaskel, D. Matoga, V. Stavila, *Chem. Rev.* **2020**, *120*, 8581; b) L. Niu, T. Wu, M. Chen, L. Yang, J. Yang, Z. Wang, A. A. Kornyshev, H. Jiang, S. Bi, G. Feng, *Adv. Mater.* **2022**, *34*, 2200999; c) M. Ko, L. Mendecki, K. A. Mirica, *Chem. Commun.* **2018**, *54*, 7873.

[63] O. K. Farha, J. T. Hupp, *Acc. Chem. Res.* **2010**, *43*, 1166.

[64] J. E. Mondloch, O. Karagiaridi, O. K. Farha, J. T. Hupp, *CrystEngComm* **2013**, *15*, 9258.

[65] A. P. Nelson, O. K. Farha, K. L. Mulfort, J. T. Hupp, *J. Am. Chem. Soc.* **2009**, *131*, 458.

[66] L. Ma, A. Jin, Z. Xie, W. Lin, *Angew. Chem. Int. Ed.* **2009**, *48*, 9905.

[67] J. Espín, L. Garzón-Tovar, A. Carné-Sánchez, I. Imaz, D. Maspoch, *ACS Appl. Mater. Interfaces* **2018**, *10*, 9555.

[68] X. Su, Z. Zhong, X. Yan, T. Zhang, C. Wang, Y.-X. Wang, G. Xu, L. Chen, *Angew. Chem. Int. Ed.* **2023**, *62*, e202302645.

[69] a) S. Gu, S. Xu, X. Song, H. Li, Y. Wang, G. Zhou, N. Wang, H. Chang, *ACS Appl. Mater. Interfaces* **2022**, *14*, 50815; b) J. Zhang, G. Zhou, H.-I. Un, F. Zheng, K. Jastrzembski, M. Wang, Q. Guo, D. Mücke, H. Qi, Y. Lu, Z. Wang, Y. Liang, M. Löffler, U. Kaiser, T. Frauenheim, A. Mateo-Alonso, Z. Huang, X. Feng, R. Dong, *J. Am. Chem. Soc.* **2023**, *145*, 23630.

[70] M. A. Haidekker, T. P. Brady, D. Lichlyter, E. A. Theodorakis, *Bioorg. Chem.* **2005**, *33*, 415.

[71] A. Mahringer, M. Doblinger, M. Hennemann, C. Gruber, D. Fehn, P. I. Scheurle, P. Hosseini, I. Santourian, A. Schirmacher, J. M. Rotter, G. Wittstock, K. Meyer, T. Clark, T. Bein, D. D. Medina, *Angew. Chem. Int. Ed.* **2021**, *60*, 18065.

[72] M. A. Borysiewicz, J. H. Dou, I. Stassen, M. Dinca, *Faraday Discuss.* **2021**, *231*, 298.

[73] W. H. Li, K. Ding, H. R. Tian, M. S. Yao, B. Nath, W. H. Deng, Y. Wang, G. Xu, *Adv. Funct. Mater.* **2017**, *27*, 1702067.

[74] S. Zhou, X. Kong, B. Zheng, F. Huo, M. Strømme, C. Xu, *ACS Nano* **2019**, *13*, 9578.

[75] S.-J. Shin, J. W. Gittins, M. J. Golomb, A. C. Forse, A. Walsh, *J. Am. Chem. Soc.* **2023**, *145*, 14529.

[76] S. Takaishi, M. Hosoda, T. Kajiwara, H. Miyasaka, M. Yamashita, Y. Nakanishi, K. Kitagawa, K. Yamaguchi, A. Kobayashi, H. Kitagawa, *Inorg. Chem.* **2009**, *48*, 9048.

[77] Y. Kobayashi, B. Jacobs, M. D. Allendorf, J. R. Long, *Chem. Mater.* **2010**, *22*, 4120.

[78] L. E. Darago, M. L. Aubrey, C. J. Yu, M. I. Gonzalez, J. R. Long, *J. Am. Chem. Soc.* **2015**, *137*, 15703.

[79] M. L. Aubrey, B. M. Wiers, S. C. Andrews, T. Sakurai, S. E. Reyes-Lillo, S. M. Hamed, C.-J. Yu, L. E. Darago, J. A. Mason, J.-O. Baeg, F. Grandjean, G. J. Long, S. Seki, J. B. Neaton, P. Yang, J. R. Long, *Nat. Mater.* **2018**, *17*, 625.

[80] L. S. Xie, L. Sun, R. Wan, S. S. Park, J. A. DeGayner, C. H. Hendon, M. Dinca, *J. Am. Chem. Soc.* **2018**, *140*, 7411.

[81] K. Fan, J. Li, Y. Xu, C. Fu, Y. Chen, C. Zhang, G. Zhang, J. Ma, T. Zhai, C. Wang, *J. Am. Chem. Soc.* **2023**, *145*, 12682.

[82] S. Gupta, H. Tanaka, K. Fuku, H. Uchida, H. Iguchi, R. Sakamoto, H. Kobayashi, Y. Gambe, I. Honma, Y. Hirai, S. Hayami, S. Takaishi, *Inorg. Chem.* **2023**, *62*, 6306.

[83] F. Gándara, F. J. Uribe-Romo, D. K. Britt, H. Furukawa, L. Lei, R. Cheng, X. Duan, M. O'Keeffe, O. M. Yaghi, *Chem. Eur. J.* **2012**, *18*, 10595.

[84] S. S. Park, E. R. Hontz, L. Sun, C. H. Hendon, A. Walsh, T. Van Voorhis, M. Dincă, *J. Am. Chem. Soc.* **2015**, *137*, 1774.

[85] M. Usman, S. Mendiratta, S. Batjargal, G. Haider, M. Hayashi, N. Rao Gade, J.-W. Chen, Y.-F. Chen, K.-L. Lu, *ACS Appl. Mater. Interfaces* **2015**, *7*, 22767.

[86] D. Chen, H. Xing, Z. Su, C. Wang, *Chem. Commun.* **2016**, *52*, 2019.

[87] L. Qu, H. Iguchi, S. Takaishi, F. Habib, C. F. Leong, D. M. D'Alessandro, T. Yoshida, H. Abe, E. Nishibori, M. Yamashita, *J. Am. Chem. Soc.* **2019**, *141*, 6802.

[88] G. Chen, L. B. Gee, W. Xu, Y. Zhu, J. S. Lezama-Pacheco, Z. Huang, Z. Li, J. T. Babicz, S. Choudhury, T.-H. Chang, E. Reed, E. I. Solomon, Z. Bao, *J. Am. Chem. Soc.* **2020**, *142*, 21243.

[89] J. Park, A. C. Hinckley, Z. Huang, G. Chen, A. A. Yakovenko, X. Zou, Z. Bao, *J. Am. Chem. Soc.* **2020**, *142*, 20531.

[90] G. Skorupskii, M. Dincă, *J. Am. Chem. Soc.* **2020**, *142*, 6920.

[91] H. C. Wentz, G. Skorupskii, A. B. Bonfim, J. L. Mancuso, C. H. Hendon, E. H. Oriel, G. T. Sazama, M. G. Campbell, *Chem. Sci.* **2020**, *11*, 1342.

[92] X. Wu, Y. Qiu, Z. Chen, B. Guan, X. Hao, A. I. Rykov, Y. Sun, L. Liu, Y. Zou, J. Sun, W. Xu, D. Zhu, *Angew. Chem. Int. Ed.* **2020**, *59*, 20873.

[93] C. A. Peeples, D. Kober, F. J. Schmitt, P. Tholen, K. Siemensmeyer, Q. Halldorson, B. Çoşut, A. Gurlo, A. O. Yazaydin, G. Hanna, G. Yücesan, *Adv. Funct. Mater.* **2021**, *31*, 2007294.

[94] Y. Zorlu, L. Wagner, P. Tholen, M. M. Ayhan, C. Bayraktar, G. Hanna, A. O. Yazaydin, Ö. Yavuzçetin, G. Yücesan, *Adv. Opt. Mater.* **2022**, *10*, 2200213.

[95] G. Skorupskii, K. N. Le, D. L. M. Cordova, L. Yang, T. Chen, C. H. Hendon, M. Q. Arguilla, M. Dincă, *Proc. Natl. Acad. Sci. USA* **2022**, *119*, e2205127119.

[96] X. Li, R. Anderson, H. C. Fry, S. M. Pratik, X. Wu, S. Goswami, T. G. Allen, J. Yu, S. S. Rajasree, C. J. Cramer, G. Rumbles, D. A. Gómez-Gualdrón, P. Deria, *ACS Appl. Mater. Interfaces* **2023**, *15*, 28228.

[97] G. Xing, J. Liu, Y. Zhou, S. Fu, J. J. Zheng, X. Su, X. Gao, O. Terasaki, M. Bonn, H. I. Wang, L. Chen, *J. Am. Chem. Soc.* **2023**, *146*, 8979.

[98] K. Wada, K. Sakaushi, S. Sasaki, H. Nishihara, *Angew. Chem. Int. Ed.* **2018**, *57*, 8886.

[99] Q. Jiang, P. Xiong, J. Liu, Z. Xie, Q. Wang, X. Q. Yang, E. Hu, Y. Cao, J. Sun, Y. Xu, L. Chen, *Angew. Chem. Int. Ed.* **2020**, *59*, 5273.

[100] Z. Wu, D. Adekoya, X. Huang, M. J. Kiefel, J. Xie, W. Xu, Q. Zhang, D. Zhu, S. Zhang, *ACS Nano* **2020**, *14*, 12016.

[101] J. M. Wrogemann, M. J. Luther, P. Barmann, M. Lounasvuori, A. Javed, M. Tiemann, R. Golnak, J. Xiao, T. Petit, T. Placke, M. Winter, *Angew. Chem. Int. Ed.* **2023**, *135*, e202303111.

[102] Y. Xiao, Y. Xiang, S. Guo, J. Wang, Y. Ouyang, D. Li, Q. Zeng, W. Gong, L. Gan, Q. Zhang, S. Huang, *Energy Storage Mater.* **2022**, *51*, 882.

[103] Z. Zhu, Y. Zeng, Z. Pei, D. Luan, X. Wang, X.-W. Lou, *Angew. Chem. Int. Ed.* **2023**, *135*, e202305828.

[104] F. Li, X. Zhang, X. Liu, M. Zhao, *ACS Appl. Mater. Interfaces* **2018**, *10*, 15012.

[105] Q. Lv, Z. Zhu, Y. Ni, B. Wen, Z. Jiang, H. Fang, F. Li, *J. Am. Chem. Soc.* **2022**, *144*, 23239.

[106] Q. Lv, Z. Zhu, S. Zhao, L. Wang, Q. Zhao, F. Li, L. A. Archer, J. Chen, *J. Am. Chem. Soc.* **2021**, *143*, 1941.

[107] L. Majidi, A. Ahmadiparidari, N. Shan, S. Kumar Singh, C. Zhang, Z. Huang, S. Rastegar, K. Kumar, Z. Hemmat, A. T. Ngo, P. Zapol, J. Cabana, A. Subramanian, L. A. Curtiss, A. Salehi-Khojin, *Small* **2022**, *18*, e2102902.

[108] a) K. W. Nam, S. S. Park, R. Dos Reis, V. P. Dravid, H. Kim, C. A. Mirkin, J. F. Stoddart, *Nat. Commun.* **2019**, *10*, 4948; b) R. R. Kapaev, I. S. Zhidkov, E. Z. Kurmaev, K. J. Stevenson, P. A. Troshin, *Chem. Commun.* **2020**, *56*, 1541.

[109] K. Kon, K. Uchida, K. Fuku, S. Yamanaka, B. Wu, D. Yamazui, H. Iguchi, H. Kobayashi, Y. Gambe, I. Honma, S. Takaishi, *ACS Appl. Mater. Interfaces* **2021**, *13*, 38188.

[110] Z. Wu, D. Adekoya, X. Huang, M. J. Kiefel, J. Xie, W. Xu, Q. Zhang, D. Zhu, S. Zhang, *ACS Nano* **2020**, *14*, 12016.

[111] J. Yan, J. Cui, M. Xie, G. Z. Yang, D. S. Bin, D. Li, *Angew. Chem. Int. Ed.* **2021**, *60*, 24467.

[112] C. Li, C. Zhang, K. Wang, F. Yu, J. Xie, Q. Zhang, *Chem. Eng. J.* **2022**, *431*, 133234.

[113] L. Guo, J. Sun, W. Zhang, L. Hou, L. Liang, Y. Liu, C. Yuan, *ChemSusChem* **2019**, *12*, 5051.

[114] A. Nazir, H. T. T. Le, A.-G. Nguyen, C.-J. Park, *Electrochim. Acta* **2021**, *389*, 138750.

[115] X. Yin, X. Chen, W. Sun, L.-P. Lv, Y. Wang, *Energy Storage Mater.* **2020**, *25*, 846.

[116] S. Gu, Z. Bai, S. Majumder, B. Huang, G. Chen, *J. Power Sources* **2019**, *429*, 22.

[117] C. Li, X. Lou, M. Shen, X. Hu, Z. Guo, Y. Wang, B. Hu, Q. Chen, *ACS Appl. Mater. Interfaces* **2016**, *8*, 15352.

[118] Y. Cai, W. Wang, X. Cao, L. Wei, C. Ye, C. Meng, A. Yuan, H. Pang, C. Yu, *Adv. Funct. Mater.* **2022**, *32*, 2109927.

[119] Z. Wang, G. Wang, H. Qi, M. Wang, M. Wang, S. Park, H. Wang, M. Yu, U. Kaiser, A. Fery, S. Zhou, R. Dong, X. Feng, *Chem. Sci.* **2020**, *11*, 7665.

[120] H. Nagatomi, N. Yanai, T. Yamada, K. Shiraishi, N. Kimizuka, *Chem. Eur. J.* **2018**, *24*, 1806.

[121] R. R. Kapaev, S. Olthof, I. S. Zhidkov, E. Z. Kurmaev, K. J. Stevenson, K. Meerholz, P. A. Troshin, *Chem. Mater.* **2019**, *31*, 5197.

[122] K. Wada, H. Maeda, T. Tsuji, K. Sakaushi, S. Sasaki, H. Nishihara, *Inorg. Chem.* **2020**, *59*, 10604.

[123] M. E. Ziebel, C. A. Gaggioli, A. B. Turkiewicz, W. Ryu, L. Gagliardi, J. R. Long, *J. Am. Chem. Soc.* **2020**, *142*, 2653.

[124] J. Xie, X. F. Cheng, X. Cao, J. H. He, W. Guo, D. S. Li, Z. J. Xu, Y. Huang, J. M. Lu, Q. Zhang, *Small* **2019**, *15*, 1903188.

[125] H. Dong, H. Gao, J. Geng, X. Hou, S. Gao, S. Wang, S. Chou, *J. Phys. Chem. C* **2021**, *125*, 20814.

[126] H. Chen, Y. Xiao, C. Chen, J. Yang, C. Gao, Y. Chen, J. Wu, Y. Shen, W. Zhang, S. Li, F. Huo, B. Zheng, *ACS Appl. Mater. Interfaces* **2019**, *11*, 11459.

[127] Y. Zang, F. Pei, J. Huang, Z. Fu, G. Xu, X. Fang, *Adv. Energy Mater.* **2018**, *8*, 1802052.

[128] D. Cai, M. Lu, L. Li, J. Cao, D. Chen, H. Tu, J. Li, W. Han, *Small* **2019**, *15*, e1902605.

[129] H. J. Kim, Y. Kim, J. Shim, K. H. Jung, M. S. Jung, H. Kim, J.-C. Lee, K. T. Lee, *ACS Appl. Mater. Interfaces* **2018**, *10*, 3479.

[130] F. Wang, Z. Liu, C. Yang, H. Zhong, G. Nam, P. Zhang, R. Dong, Y. Wu, J. Cho, J. Zhang, X. Feng, *Adv. Mater.* **2020**, *32*, e1905361.

[131] B. Wang, J. Li, M. Ye, Y. Zhang, Y. Tang, X. Hu, J. He, C. C. Li, *Adv. Funct. Mater.* **2022**, *32*, 2112072.

[132] K. Fan, C. Fu, Y. Chen, C. Zhang, G. Zhang, L. Guan, M. Mao, J. Ma, W. Hu, C. Wang, *Adv. Sci.* **2023**, *10*, 2205760.

[133] Y. Chen, Q. Zhu, K. Fan, Y. Gu, M. Sun, Z. Li, C. Zhang, Y. Wu, Q. Wang, S. Xu, J. Ma, C. Wang, W. Hu, *Angew. Chem. Int. Ed.* **2021**, *133*, 18917.

[134] L. Wang, Y. Ni, X. Hou, L. Chen, F. Li, J. Chen, *Angew. Chem. Int. Ed.* **2020**, *132*, 22310.

[135] C. Fang, Y. Huang, L. Yuan, Y. Liu, W. Chen, Y. Huang, K. Chen, J. Han, Q. Liu, Y. Huang, *Angew. Chem. Int. Ed.* **2017**, *56*, 6793.

[136] Y. Wu, Y. Chen, M. Tang, S. Zhu, C. Jiang, S. Zhuo, C. Wang, *Chem. Commun.* **2019**, *55*, 10856.

[137] W. Zhou, S. Lv, X. Liu, Y. Li, J. Liu, *Chem. Commun.* **2019**, *55*, 11207.

[138] S. S. Shinde, C. H. Lee, J.-Y. Jung, N. K. Wagh, S.-H. Kim, D.-H. Kim, C. Lin, S. U. Lee, J.-H. Lee, *Energy Environ. Sci.* **2019**, *12*, 727.

[139] O. A. Kraevaya, E. V. Shchurik, P. A. Troshin, *Physica Status Solidi A* **2020**, *217*, 1901050.

[140] D. Xiong, X. Deng, Z. Cao, S. Tao, Z. Song, X. Xiao, W. Deng, H. Hou, G. Zou, X. Ji, *Energy Environ.* **2023**, *6*, e12521.

[141] A. S. Rosen, V. Fung, P. Huck, C. T. O'Donnell, M. K. Horton, D. G. Truhlar, K. A. Persson, J. M. Notestein, R. Q. Snurr, *npj Computational Materials* **2022**, *8*, 112.

[142] C. Li, X. Sun, Y. Yao, G. Hong, *Materials Today Nano* **2021**, *13*, 100105.